Citation
Ngo, T.T. and Pham, T.M. and Hao, H. 2020. Ductile and dry exterior joints using CFRP bolts for moment-resisting frames. Structures. 28: pp. 668-684. http://doi.org/10.1016/j.istruc.2020.09.020

Ductile and Dry Exterior Joints Using CFRP Bolts for Moment-Resisting Frames

Tuan T. Ngo[1], Thong M. Pham[2]*, and Hong Hao[3]*

Abstract

This study proposes a new dry joint type for moment-resisting frames by using carbon fibre reinforced polymer (CFRP) bolts and plates. This is one of very rare studies focusing on the potential of using CFRP bolts to connect the precast beam-column joints. CFRP bolts have been recognized for their good performances, which could effectively resolve a very costly issue of corrosion in the common dry joints using steel bolts, plates, and tendons. Cyclic loading was applied to test four specimens until 85% of the post-peak load. The results indicated that the proposed dry joints showed better performances compared to the reference monolithic joint in the load-carrying capacity, energy dissipation, and stiffness, which increased by 27-61%, 45-75%, and 27-55%, respectively. Particularly, drift ratio of all the proposed joints exceeded 3%, which is higher than the requirements for ductile joints in various standards. The ductility of the proposed joints was also more preferable than the reference monolithic joint (i.e. 2.2 vs 2.4). These exciting results suggest that these new dry joints can be plausibly applied to prefabricated constructions in non-seismic and seismic-prone areas. In addition, the proposed dry joints offer numerous advantages, compared to the traditional monolithic joints, in terms of construction time and construction-quality control.

Keywords: Fibre Reinforced Polymer (FRP) bolts; Corrosion; Prestress bolts; Ductile precast joint; Cyclic load; Concrete-end-plates; Precast exterior joint.

[1] PhD Scholar, Center for Infrastructural Monitoring and Protection, School of Civil and Mechanical Engineering, Curtin University, Kent Street, Bentley, WA 6102, Australia and The Faculty of Engineering and Technology, Quy Nhon University, 170 An Duong Vuong Street, Binh Dinh, Viet Nam. Email: tangtuan.ngo@postgrad.curtin.edu.au

[2] Lecturer, Center for Infrastructural Monitoring and Protection, School of Civil and Mechanical Engineering, Curtin University, Kent Street, Bentley, WA 6102, Australia (**Corresponding author*). Email: thong.pham@curtin.edu.au

[3] John Curtin Distinguished Professor, Center for Infrastructural Monitoring and Protection, School of Civil and Mechanical Engineering, Curtin University, Kent Street, Bentley, WA 6102, Australia (**Corresponding author*). Email: hong.hao@curtin.edu.au

1. Introduction

Beam-column joints play a vital role in the behaviours of moment-resisting frames. They support the development of the ultimate capacity of adjacent members. This characteristic can only be achieved when the joints between beams and columns have sufficient strength and stiffness so that internal forces between members could transmit together. Lessons from various earthquakes have indicated that if the joints are destroyed, the building would collapse, although beams and columns are still undamaged [1, 2].

Most of existing studies have focused on monolithic, wet, or hybrid joints [3-6] due to their good performance in peak load, stiffness, energy dissipation, ductility, and hysteretic behaviours. However, there have been still some disadvantages in these joint types, such as longer construction time, higher construction cost, more difficulties to control construction quality, and negative effects on the environment as compared to dry joints. Beams and columns in the dry joints are cast in factories before they are assembled in construction sites. Therefore, the application of dry joints could effectively resolve the above disadvantages of monolithic, wet, or hybrid joints [7, 8]. Nevertheless, the application of dry joints in reality is still limited compared to monolithic joints due to disadvantages related to strength, ductility, and corrosion resistance. Since beams and columns are cast separately and are connected later by bolts and tendons, dry joints are usually weaker than monolithic joints. For example, dry joints using cleat angles and stiffeners have not been recommended for use in earthquake-prone regions [9]. In precast concrete structures, especially with traditional dry joints, corrosion is more likely to occur because connecting elements might be not protected properly by concrete. The corrosion of the connecting elements leads to deterioration or even destruction of the entire buildings [10, 11]. Additionally, the expenditure to maintain and repair deteriorated members in some circumstances can be incredibly more costly than the original new ones [12, 13].

Meanwhile, fibre reinforced polymers (FRP) have gained its increasing popularity in civil engineering because they offer favourable features, such as lightweight, high strength, easy implementation, fatigue resistance, and good corrosion resistance [14, 15]. Recently, FRP bolts have been introduced to the market but its application for structural engineering is still limited. GFRP and CFRP bolts are the popular types, in which GFRP bolts are more favoured because they are more cost-effective [16, 17]. The use of FRP bolts has not been popular in construction because the shear capacity of these bolts is relatively low as compared to steel bolts. FRP bolts are very strong in tension but weak in shear [18, 19].

Recently, CFRP and Basalt tendons have been applied in precast segmental concrete beams and normal beams to replace steel tendons for effective mitigation of corrosion problems [20, 21]. The functions of FRP tendons and FRP bolts are similar in tensile behavior and prestress needs to be applied to these bolts/tendons before applying external loads. However, the application of FRP tendons in the structures is quite challenging compared to steel tendons due to the anchorage problem. This is because of the relatively low shear and compressive capacity of FRP materials so that anchors could fail by excessive principal stresses, local crushing, and interfacial slippage [22]. Therefore, the use of conventional anchorage methods for FRP tendons is not reliable and difficult to predict anchorage failure patterns. In addition, FRP sheets have been popularly applied to strengthen beam-column joints [14, 23]. Conventional steel reinforcements were replaced by GFRP bars to minimize corrosion [18, 24]. However, most of existing studies focus on wet and hybrid joints while there are very few studies on precast beam-column joints with FRP bolts. Feroldi and Russo [25] investigated precast beam-column joints using pultruded plates and C-shape FRP bars to replace steel plates and C-shape steel bars in steel structures. Since steel bolts were used to connect the beams and columns, these joints were still susceptible to corrosion of the metal parts. To date, no publication is available in literature yet to use FRP bolts and plates to connect beam-column joints.

Among various types of concrete dry joints, the most popular type is dry joints with concrete-end-plates. In this joint type, the concrete-end-plates are used to connect the beams to the adjacent columns using steel bolts. This type of dry joints can be easily installed and post-tensioned with no required formwork. Despite their advantages, only few studies focus on the behaviours and applications of this joint [26-28]. Saqan [27] and Palmieri, Saqan [28] conducted an experiment with large-scale specimens and an analytical investigation on this dry joint type. Among the five large-scale joints studied, the internal beam-column joint with the concrete-end-plates and steel bolts showed the worst behaviours, specifically in the load-carrying capacity, drift ratio, and energy absorption capability. The experimental results indicated that the concrete-end-plates failed due to concrete crushing at the top and bottom zones. It was explained that concrete stress in compression struts reached its compressive strength at a low drift ratio of 1.5% and caused damage [27, 28]. Possibly, due to these negative results, the dry joint type using concrete-end-plates and steel bolts was overlooked. As a result, there is a lack of studies on the behaviours of this dry joint type.

It is clear from the literature that the advantages of dry joints can only be leveraged if more research is done to improve the capacities of these joints in terms of ductility, energy dissipation, stiffness, load-carrying capacity, and corrosion resistance. The current study, therefore, aims to propose dry beam-column joints for non-seismic and seismic-prone locations by using corrosion-resistant CFRP bolts to replace conventional steel bolts. The effects of thickness of the concrete-end-plates are also investigated. It is expected that the proposed dry joints yield sufficient ductility and load-carrying capacity, as well as solving the issue of corrosion effectively. The use of CFRP bolts in the proposed joints is critical to increase the lifetime of structures and reduce the construction time and maintenance costs, which helps to promote the use of these dry joints in the construction sector.

2. Experimental program

This study proposes a new corrosion-resistant joint type that exhibits sufficient strength and ductility to be used in both non-seismic and seismic-prone regions. To evaluate the dry joint performance using CFRP bolts and steel bolts under quasi-static cyclic loads, four specimens were cast and tested until failure, including a monolithic specimen (MS), a precast specimen 2 (PS2) with CFRP bolts and no steel spirals in the concrete-end-plate, a precast specimen 3 (PS3) with CFRP bolts and steel spirals, and a precast specimen 4 (SP4) with steel bolts and steel spirals. Spirals were used in the concrete-end-plate to confine concrete and improve the capacity of the concrete-end-plate and thus the joint. All the bolts in the precast specimens had the same diameter of 20 mm. Details of the specimen design and the test setup are presented in the following sections.

2.1 Design of the specimens

Four exterior beam-column joints with a scale of 1/3 of an eight-floor building were designed according to ACI 550R-96 [29] and ACI 352R-02 [30]. The design was based on the design philosophy of strong columns and weak beams. The two previous studies by Hanaor and Ben-Arroyo [26] and Saqan [27] were also used as references to design the precast beam-column joints since there have been no existing standards for the precast joints using bolts and concrete-end-plates. The columns in all the specimens had the same length of 1280 mm with a square-shaped cross-section of 200 × 200 mm^2. Four 16-mm deformed steel bars were used as longitudinal reinforcements. 10-mm stirrups with a spacing of 70 mm were used as shear reinforcements for the columns (Fig. 1).

The beams of the precast specimens had a T-shape and included two parts: (1) the concrete-end-plate and (2) Beam A. This study adopted the guides of ACI 318-11 [31] and Wight and MacGregor [32] to design Beam A. The beam section in all the specimens were reinforced with four 16-mm deformed steel bars with a reinforcement ratio of 2.2%. Additionally, 10-mm stirrups with a spacing of 70 mm were used as shear reinforcements. The dimensions of the concrete-end-plate were 350 × 150 × 200

114 mm^3 while those of Beam A was 150 × 150 × 520 mm^3 as shown in Fig. 1. According to Saqan [27],
115 the capacity of the precast beam-column joint using the concrete-end-plates and steel bolts was
116 comparably low since the crushing of the concrete appeared at the concrete-end-plate at a low drift
117 ratio of 1.5 %. Therefore, in this research, 8-mm steel spirals at a spacing of 30 mm were used to
118 confine the concrete and increase the compressive strength at the concrete-end-plates (see Fig. 2).
119 This design was expected to improve the capacity of these precast beam-column joints.

120 To evaluate the effectiveness of the steel spirals, it is necessary to determine the exact strength of the
121 concrete in the compressive zone during the test. Aluminium bars with a diameter of 6.1 mm were
122 placed in the assumed direction of the concrete struts. Strain gauges were stuck to these bars to
123 monitor the concrete strain as shown in Fig. 2. A cutting machine was used to create notches on the
124 aluminium bars. These notches helped to increase the bond between the concrete and the aluminium
125 bars. The concrete cover of all the beams and columns was 35mm as required in ACI 318-11 [31].
126 Details of all the reinforcements, steel spirals, and CFRP bolts are shown in Tables 1 and 2.

127 The most challenging issue in the prefabrication of these precast specimens was to ensure that the
128 four bolts went through the beams and the columns smoothly when assembling the joints. To resolve
129 this issue, the formworks for columns and beams were set up together as real joints. The holes inside
130 the beams and columns were created by embedding plastic tubes with an outside diameter of 21 mm
131 into the steel cages before the concrete was poured. Details of plastic tube disposition are shown in
132 Fig. 2. In the two previous studies [26, 27], the tensile force in the bolts, a crucial parameter to
133 determine the behaviours of the proposed joint type, was not reported. In the current experiment, two
134 20-ton load cells were used to measure the tensile forces in the bolts as shown in Fig. 3.

135 **2.2 Mechanical properties of materials**

136 Concrete properties are determined according to AS 1012.8.1-14 [33] and AS 1012.9.1-14 [34] as the
137 averaged values from three 100 × 200 mm cylinders. The average compressive strength (f'_c) and

tensile strength (f_{ct}) of concrete on the testing day was 38.4 MPa and 3.8 MPa, respectively. The ultimate tensile strengths of the reinforcements were 522 MPa for 8-mm bars, 675 MPa for 10-mm bars, and 706 MPa for 16-mm bars. Other properties of these steel bars and aluminium bars which were provided by the manufacturer are presented in Table 1.

CFRP bolts were supplied by J and R Metalwork Industry CO. [35]. As informed by the manufacturers, GB/T 1447-05 [36] was used to evaluate the mechanical properties of CFRP bolts. The number of samples for the testing was 20-30 with a length of 800-1000 mm. The tensile strength, shear strength, and elastic modulus of 20-mm CFRP bolts were 850 MPa, 160 MPa, and 100 GPa, respectively. It is noted that the capacity of the entire bolts is restrained primarily by the capacity of the nuts with the ultimate load of 100 kN for the 20-mm bolts. The detailed properties of CFRP bolts, nuts, and plates are presented in Table 2. In addition, M20-metric steel bolts with class 8.8 had the proof load, yield stress, ultimate strength of 580 MPa, 640 MPa, and 800 MPa, respectively [37].

Strain gauges with a length of 5 mm were bonded to stirrups, longitudinal reinforcements, and aluminium bars to measure the strain of reinforcements and the assumed concrete struts. Additionally, to measure the strain of concrete in diagonal struts of the concrete-end-plate, 60-mm strain gauges were glued on these estimated areas. Detailed strain gauges are presented in Figs. 2 and 3.

2.3 Specimen preparation and test setup

A steel brush and a compressed air gun were used to clean the holes and remove dust before the test setup. The column was the first to be connected to the reaction frame. Then, the beam was lifted by a forklift and connected to the column with four bolts. The setup process in this experiment is also applicable in reality. Four bolts with a diameter of 20 mm went through the four holes with a diameter of 21 mm on the beams and columns. CFRP or steel plates were placed into the bolts before nuts were tightened by a torque wrench to avoid concentrated stress around the bolts. According to the

information provided by the manufacturer, 80 Nm of torque was recommended to apply to the CFRP nuts.

For the test setup, a hydraulic jack was used to apply the vertical restrain on the column top with an axial force of 15 kN ($0.01f_c'A_c$). Since the effect of the axial force is not the focus of this study, it was maintained as low as possible. It was reported in a previous study that higher axial force is beneficial to the capacity of the joints [38]. Therefore, this study aims to investigate the most unfavorable case of joints. Another hydraulic jack was used to apply the vertical quasi-static cyclic loading at the beam tip. The jack was installed at 650 mm from the column center. The details of the test setup are presented in Fig. 4. The beam-column joints were tested under cyclic loading until 85% post-peak load. The loading history, which was based on ACI T1.1-01 [39], is shown in Fig. 5. Due to the time limitation, two load cycles were conducted at each loading level under displacement control at the level of 6-9 mm/min.

2.4 Experimental results and discussion

2.4.1 General behaviours and failure patterns

Fig. 6 shows the failure modes of all the tested specimens. All the precast specimens experienced no visible cracks on the columns. As expected, the column showed good performance without any failure, which satisfied the criteria for weak beams-strong columns. The maximum tensile force in the CFRP bolts did not reach its strength limit. For example, the maximum tensile force of the CFRP bolts in Specimen PS3 was only 34% of its ultimate tensile force (see Table. 2). Therefore, no failure was observed in the CFRP bolts. Additionally, although no corbels or brackets were used for all the precast specimens, no slips were recorded during the tests, which was demonstrated by LVDT data (almost zero). The main failure of Specimens MS and PS4 occurred at the beams whereas Specimens PS2 and PS3 exhibited failure at the joints. More observations and discussions on the failure modes will be presented in Section 2.4.2.

185 The reference Specimen MS exhibited flexural cracks on the beam and inclined cracks in the joint.
186 The vertical flexural cracks were observed firstly on the beam when the beam soffit was in tension.
187 These cracks were located at distances of 1, 100, and 220 mm from the face of the column at ±0.7 %
188 (±4.0 mm) drift ratio corresponding to the tip displacement of ±4.0 mm. For convenience, hereby the
189 number in the bracket after the drift ratio shows the corresponding tip displacement. There were no
190 shear cracks on the beam as shown in Fig. 6 (MS). Then, the inclined cracks appeared and propagated
191 into the joint zone after 1% drift ratio. These inclined cracks firstly formed in the middle of the joint
192 before developing toward two corners of the column. The maximum width of the inclined crack
193 achieved approximately 1.5 mm at 5.5% drift ratio. Minor crushing of concrete occurred at the fixed-
194 end when drift ratio reached 2%. The monolithic specimen MS achieved the maximum capacity at
195 the drift ratio of 5.0%. Eventually, the crushing of concrete and vertical cracks at the fixed end caused
196 the failure of Specimen MS.

197 As shown in Fig. 6, Specimens PS2 and PS3 exhibited the same failure patterns and the same crack
198 development modes. The flexural crack initially formed at the fixed end at ±0.5% drift ratio
199 (±2.5mm). When drift ratio reached ±0.6% (±3.3 mm), the inclined cracks had a tendency to
200 propagate into the middle zone of the concrete-end-plate. At the initial stage, two vertical cracks at
201 the fixed end were formed because the tensile strain of concrete at this section reached its maximum
202 value due to sufficient bending moments. In the following stages, the longitudinal reinforcements
203 started to significantly contribute to the flexural resistance and did not show considerable damage but
204 some cracks. Meanwhile, inclined cracks gradually developed in the middle zone of the concrete-
205 end-plate with an increase of the inclined angle (see Fig. 6). These inclined cracks initiated in the
206 middle and then developed to the top and bottom of the concrete-end-plate and caused the failure.

207 Fig. 7 shows the data of strain gauges of the longitudinal reinforcements and the concrete-end-plates
208 in all the tested specimens. The dots in this figure indicate their maximum strain at each cycle. The
209 data of strain gauges at drift ratio of 3.0% (±16.4 mm) on Specimen PS3 in Figs 7 indicate that the

strain of longitudinal reinforcements (2559 με) reached the yielding point (2980 με) and the tensile strain of concrete (1334 με) exceeded the ultimate tensile strain (131 με). The maximum tensile strain of concrete was determined based on its tensile strength (f_{ct}). Therefore, two main inclined cracks (see red curves on Figs. 6) significantly opened with a width of approximately 2-3 mm, which caused the main failure for Specimens PS2 and PS3. Additionally, there were no shear cracks on Beam A of Specimens PS2 and PS3.

Specimen PS4 showed different failure patterns as compared to Specimens PS2 and PS3. The two inclined cracks, which formed a V-shape, initially appeared from the two corners between Beam A and the concrete-end-plate (see the red curve in Fig. 6 (PS4)). These inclined cracks occurred soon after the load was applied at the beam tip at 0.3% drift ratio (±1.65 mm). At 0.8% drift ratio, the inclined cracks developed from the fixed end into the middle areas of the concrete-end-plate. It is different from Specimens PS2 and PS3 due to the effects of the prestress level of the bolts. The inclined cracks of Specimen PS4 occurred mainly in the middle and only one inclined crack appeared at the top and bottom of the concrete-end-place after achieving the peak load of 50.3 kN with 3.0% drift ratio (see the pink curves in Fig. 6 (PS4)). The prestress level of Specimen PS4 was higher than those of Specimens PS2 and PS3 by approximately 12.4 and 7.8 times, respectively. The high prestress level in the bolts might have helped to improve the confined capacity of the concrete in the top and bottom zones of the concrete-end-plate [26]. From 2.8% drift ratio, the concrete on the top and bottom of the concrete-end-plate began to crush, and the red curve crack opened approximately 4-5 mm, which caused the main failure in Specimen PS4 as shown in Fig. 6 (PS4)).

Fig. 7 shows the strain at the surface of the concrete-end-plate while Fig 8 presents the strain inside the concrete-end-plate was measured by the aluminium bars at the possible struts. In Fig. 8, the maximum measured strain inside the middle zone was much higher than that at the top and bottom zones of the concrete-end-plates. For instance, the maximum measured tensile strain inside the middle zone and the top zone at 4% drift ratio of Specimen PS4 was 4971 με and 314 με, respectively.

Therefore, it might be concluded that the tensile stress inside the top and bottom zones was lower than that inside the middle zone. As a result, the proposed dry joints failed differently from those in the previous study by Saqan [27] who reported that the main failure was the compression strut at the top and bottom zone of the concrete-end-plate. To further analyse the failure mechanism, Fig. 9 presents a sketch of force paths in the concrete-end-plate, T_1 vs T_2 and T_3 are the tensile forces of the bolts and reinforcements and T_4, q_1 vs q_2, and q_3 are the compressive forces of the reinforcements, CFRP plates, and bottom zones. Theoretically, there are two possibilities for the failure of the joints governed by either compressive or tensile strength of concrete [32]. The data of strain gauges in Figs. 7 (b) and 8 indicate that the compressive strain in the compression struts of the concrete-end-plate was relatively small (< 110 με) and did not reach the maximum compressive strain of concrete, whereas the tensile strain of concrete (> 1334 με) well exceeded its maximum tensile strain (131 με). Therefore, it is suggested that the major cracks and failure of these precast specimens were caused by the tensile strain of concrete. This mechanism could be explained by the two effects: (1) the angle of possible struts and (2) the bond between reinforcements and concrete. There were two possible struts (i.e., Struts AB and AC) that might occur on concrete-end-plates as shown in Fig.9. The angle of Strut AB was quite small (approximately 34^0) and the bond stress (b in Fig. 9) between the reinforcements and the concrete had the tendency to resist the tensile force (T_3) in the reinforcements. Therefore, the tensile force (T_3) in the reinforcements at node B was low which led to the low compressive stress of concrete around node B. For Strut AC, it had a larger angle (50^0) and higher compressive stress as compared to that of Strut AB. Meanwhile, the failure of Specimens PS2 and PS3, as shown in Fig. 6, reveals that the red inclined cracks were established due to the tensile stress. From observations during the tests and the above analyses, it could be concluded that tensile cracks (AB and AC) caused the failure of the specimens.

2.4.2 Hysteretic behaviours

The hysteretic responses of all the specimens were almost symmetrical in both the push and pull directions (see Fig. 10) because both the top and bottom reinforcements in the beams were similar, with a diameter of 16 mm. However, the hysteretic curves were asymmetrical after the peak loads due to large and irreversible deformation, which is consistent with the results of the previous studies [27, 28]. Linear responses were observed in the envelope curves of all the precast specimens until 3% drift ratio. These responses were due to the linear responses of the CFRP bolts and steel bolts during the tests. In addition, the longitudinal reinforcements did not yield until 3% drift ratio (see Fig. 7), thus the main failure of the precast specimens was governed by the concrete properties. After this stage, the load started to decrease. Various cracks on the concrete-end-plates caused a significant reduction in the load-carrying capacity after 3% drift ratio. From 4% drift ratio, the envelope curves had a tendency to remain constant as indicated in Fig. 11. This performance could be explained with a reference to the strength hardening of the reinforcements. Stresses in the reinforcements still increased after reaching peak load, so the failure shifted from the joint to the beam after 4% drift ratio as also observed in the previous study [18].

To further understand the behaviours of all the specimens, the maximum design loads of the beams were estimated and presented in Fig. 11. Design loads of 28 kN and 44 kN were applied to the monolithic beam and precast beams, respectively. Specimens MS and PS4 reached their peak loads of 32.3 kN at 5% drift ratio and 50.3 kN at 3% drift ratio. These maximum loads were higher than the estimated capacities of the corresponding beams. This variation might result from the difference between the nominal tensile strength and the actual strength of the reinforcements. Taken all the above results together, it is clear that the main failure of Specimens MS and PS4 occurred at the beams, whereas that of Specimens PS2 and PS3 occurred at the joints, as discussed in section 2.4.1.

In general, the responses of Specimen MS showed nonlinear behaviours from 1% drift ratio until failure. Up to 1% drift ratio, Specimen MS exhibited elastic behaviours and dissipated little energy

because there was no evidence of a significant pinching and stiffness degradation. It is noted that the pinching indicates the energy dissipation capacity of specimens and it often occurs when there is a significant variation of the area inside hysteresis loops. After 1% drift ratio, pinching continuously increased due to the crack developments. Specimen MS began to yield at 2.7% drift ratio before reaching the maximum load at 5% drift ratio. From 5% to 6.5% drift ratio, the load capacity continuously dropped and the Specimen MS was damaged at 6.5% drift ratio. Until the end of the test, the longitudinal reinforcements in Specimen MS did not yield as shown in Fig. 7 (a) (2233 με < 2980 με) while concrete crushing at the fixed end caused a load decrease in Specimen MS. The reduction in the load-carrying capacity of all the specimens after the peak load could be mainly attributed to tensile cracks in the concrete-end-plate, crushing of concrete and flexural cracks at the fixed end, as previously explained.

2.4.3 Drift ratio and load-carrying capacities

The drift ratio is an essential parameter to evaluate the joint performances. The drift ratio is defined as follows:

$$R = \Delta / l \quad (1)$$

where Δ is the vertical displacement of the beam at the loading point and l is the distance from the loading point to the column face (l = 550 mm).

The drift ratio of a monolithic beam-column joint is reported to range approximately from 4% to 5%, which well satisfies the requirements of many standards. For example, ACI T1.1-01 [39], CSA A23.3-07 [40], and ASCE 41-06 [41] require drift ratio of 3.5%, 2.5% and 2% to ensure the life safety in earthquake-prone regions, respectively. For drift ratio of dry joints with concrete-end-plates and steel bolts, previous studies reported a value of 1.5% [27]. Therefore, the application of this dry joint type is still limited in earthquake-prone regions. Interestingly, the drift ratio of the currently tested specimens was satisfactory to be applied in earthquake-prone regions.

Table 3 shows the peak loads and the corresponding drift ratios of all the specimens. In general, the proposed dry joints showed good performances including drift ratio and load-carrying capacities as compared to those from the previous studies [26-28]. Specimen MS exhibited a ductile load-displacement response with the highest drift ratio of 5%, corresponding to the average peak load of 29.1 kN. This peak load is the lowest load-carrying capacity among all the tested specimens. All the precast specimens exhibited the same drift ratio of 3% at the peak loads. This value was higher than 2.5% and 2% required by CSA A23.3-07 [40], and ASCE 41-06 [41], respectively, to ensure life safety. Specimen PS2 reached the peak load of 39.5 kN at a drift ratio of 3%, which was 35.8% higher than that of the Specimen MS. For Specimens PS3 and PS4, the maximum loading capacities were also significantly increased with an average peak load of 36.8 kN and 46.8 kN, respectively, which were 26.6% and 61.2%, higher than that of Specimen MS.

In the previous study by Saqan [27], which investigated the same kind of joints, the failure occurred at the compression strut at the top and bottom zones of the concrete-end-plate. Therefore, the current study used steel spirals to confine concrete in this region and thus improve the load-carrying capacity and the drift ratio. Interestingly, the ultimate load and the drift ratio of Specimens PS2 and PS3 were almost the same, indicating that the use of spirals did not improve the performances of the joints. This phenomenon can be explained by the change of the failure modes. The precast specimens in this study failed due to tensile cracks of concrete in the middle zone of the concrete-end-plate which was different from the previous study [27]. The change in the failure modes was discussed in the section of 2.4.2. Meanwhile, Specimen PS4 with steel bolts had the same drift ratio of 3% but the higher maximum load (27.2%) as compared to those of Specimen PS3 with CFRP bolts. According to previous studies [7, 42, 43], high prestress levels improved the maximum load of joints. Therefore, the improvement in the ultimate load of the specimen with steel bolts was attributed to the prestress level in the bolts. Due to low torsion resistance, the CFRP bolts were prestressed at a lower force than

the steel bolts (6.5 kN vs 51 kN). Further study is necessary to investigate the effect of these parameters on the load-carrying capacity of joints.

2.4.4 Ductility of joints

Ductility is a crucial parameter to evaluate the bearing capacity of a building under earthquake loading. High ductility considerably minimises a reduction in strength and brittle failure of a building. In addition, ductility significantly affects the energy dissipation capacity of structures during inelastic deformations. In this study, the ductility is defined as the ratio of the ultimate displacement (Δ_u) to displacement at the yield loads (Δ_y), as presented in Eq. 2 [44]:

$$\mu = \Delta_u/\Delta_y \quad (2)$$

The yielding deformation in a reinforced concrete structure is determined inconsistently in different studies since the relationship between the load and displacement does not exhibit a clear yielding point due to the nonlinear behaviours of materials [44]. In this study, the yield displacement is determined at the point corresponding to the 75% of the ultimate load H_u while the ultimate displacement corresponds to the displacement at 85% the post-peak load as shown in Fig. 12 [45].

In the current study, the maximum displacement of Specimens PS3 and PS4 stopped at 27.6 mm and 28.1 mm due to the limitation of the hydraulic jack, which corresponded to 90% peak load. Therefore, the ultimate displacement of Specimens PS3 and PS4 was determined corresponding to the 90% of the peak load. The load-carrying capacity of Specimens PS3 and PS4 had a tendency to remain unchanged in the push direction from 4% drift ratio until the end of the tests due to the change of failure mode from the joints into the beams. Therefore, the ultimate displacements of Specimens PS3 and PS4 were quite high, preventing the brittle failure and giving engineers warnings before the total collapse of the structures.

Table 4 summarizes displacements at the yielding and ultimate stages of all the specimens in the two directions as well as the ductility ratio. Specimens PS3 and PS4 almost achieved the same ductility

355 level as the reference Specimen MS, which were 2.1, 2.3, 2.4, respectively. For Specimen PS2, it
356 showed less ductile behaviours than Specimens PS3, PS4, and MS, with the ductility ratio
357 approximately 19.0%, 26.1%, and 29.2% less than that of the three specimens, respectively. Specimen
358 PS3 showed a higher ductility than that of Specimen PS2 as given in Table 4 even though they had
359 quite similar designs except for the prestressing force and steel spirals. This difference results from
360 the varied ultimate displacements. Although the ultimate displacement of Specimen PS3 (27.5 mm)
361 was calculated at 90% of the post-peak load, it was still higher than that of Specimen PS2 (22.4 mm)
362 at 85% of the post-peak load. This result was because the load-carrying capacity of Specimen PS2
363 significantly dropped after achieving the peak load in the push direction. Furthermore, using the steel
364 spirals with an appropriate pitch helped to increase the ductility due to an increase in ultimate
365 displacement in Specimens PS3 and PS4 [46]. The ductility of Specimens PS3 and PS4 were quite
366 similar (2.1 vs 2.3) because the behaviours of these specimens were governed by concrete and steel
367 reinforcements while the CFRP bolts and steel bolts were over-designed with high capacity and were
368 not yielded up to failure. The similarity also proves that CFRP bolts can be used to replace steel bolts
369 to resolve the corrosion problem effectively.

370 2.4.5 Energy dissipation capacities and equivalent viscous damping ratio

371 In order to evaluate the energy dissipation capacity of the beam-column joints, the dissipated energy
372 and equivalent viscous damping ratio are determined based on the hysteretic loops.

373 2.4.5.1 Energy dissipation capacities

374 The energy dissipation capacity is an essential parameter to examine how effective a joint withstands
375 an earthquake loading. A beam-column joint subjected to quasi-static cyclic loading is classified as
376 ductile if a sufficient amount of energy is dissipated without a significant decline of its strength and
377 stiffness [9, 47]. The energy dissipation at a specific load cycle due to inelastic action is calculated as
378 the area enclosed (A_h) inside the hysteretic loop in that cycle. Fig. 13 presents the energy dissipation

capacity versus the drift ratio of the specimens. All the specimens exhibited similar patterns of energy dissipation from the initial stage to drift ratio of 1% because they behaved elastically up to 1% drift ratio. However, the overall dissipated energy of Specimen MS was less than that of the precast specimens from the drift ratio of 1% until failure because the area (A_h) in each cycle of Specimen MS was smaller than that of the precast specimens as shown in the hysteresis loops in Fig. 10. The energy dissipation at 4% drift ratio of Specimens PS2, PS3, and PS4 was 57.9%, 45.1%, and 74.5% higher than that of Specimen MS, respectively. Therefore, it can be concluded that the proposed dry joints showed good energy dissipation capacity and were suitable for applications in the seismic-prone regions.

2.4.5.2 Equivalent viscous damping ratio

The equivalent viscous damping ratio represents the ability in reducing the peak response amplitudes from inelastic deformation during an earthquake excitation [48]. The equivalent hysteretic damping ratio in a specific loading cycle is calculated based on the area inside an absolute load-displacement hysteresis loop A_h to 2π times the elastic strain energy absorbed in an equivalent linear elastic system as follows [48]:

$$\xi_{eq} = \frac{A_h}{2\pi V_m \Delta_m} \quad (3)$$

where V_m and Δ_m are the average peak load and displacement values in the i^{th} cycle, respectively, and *eq* stands for *equivalen*t.

The equivalent viscous damping ratio of Specimens MS, PS2, PS3, and PS4 was presented in Fig. 14. From 0.3 to 0.5% drift ratio, the equivalent viscous damping ratio of Specimens MS, PS2, and PS3 significantly dropped while that of Specimen PS4 increased slightly. This phenomenon was because there was a high bending moment in Specimen MS and low prestress level in CFRP bolts of Specimens PS2 and PS3 which caused a higher initial displacement at an early stage if compared to Specimen PS4.

Up to the drift ratio of 2%, the reference Specimen MS showed a higher equivalent viscous damping ratio than Specimens PS3 and PS4. At the drift ratio of 2.5%, the equivalent viscous damping ratio of Specimens PS2, PS3, and PS4 was almost equal and higher than that of Specimens MS. However, when the drift ratio is greater than 2.5%, the equivalent viscous damping ratio of all the specimens slightly increased and all the precast specimens exhibited a higher equivalent viscous damping ratio than that of Specimen MS. This reduction of Specimen MS was attributed to pinching in the curves, concrete crushing, and shear stress, which contributed to narrowing the hysteresis loop.

2.4.6 Stiffness degradation

Stiffness degradation of specimens under quasi-static loading is usually defined by the secant stiffness changes of the load-displacement curves. However, when connecting the push and pull peak of each cycle in the cyclic tests, the line does not go through the origin. In the current study, the effective stiffness was utilized to evaluate the stiffness degradation of the specimens in the cyclic tests. The slope of the line, which connected the push and pull peak loads, was used to determine the effective stiffness at each drift ratio (Fig. 15). The stiffness of all the specimens monotonically declined with the increase in the applied load. This observation is due to the numerous cracks formed at the concrete-end-plates and the crushes of concrete as shown in Fig. 6. The comparisons in the effective stiffness degradation among all the specimens are shown in Fig. 16.

In general, all the precast specimens showed higher effective stiffness than Specimen MS until the drift ratio reached 4% because *EI/l* ratio of all the precast specimens was higher than that of Specimen MS (where *EI* and *l* are the flexural rigidity and the length of a member, respectively). The effective stiffness of all the specimens continuously reduced from the beginning of the test although the envelope curves (Fig. 11) showed nearly linear responses in the initial stage. This phenomenon is possible because the development of concrete cracks occurred early in this stage (Fig. 17). Additionally, the data of strain gauges at 0.5% drift ratio also indicated that the strain of concrete exceeded the value of $30\%\varepsilon_c^{'}$, so the concrete started to experience nonlinear responses. The stiffness

428 degradation trends of Specimens PS2 and PS3 were quite similar to each other, from drift ratio of 1%
429 to 4%. The initial stiffness at 0.3% drift ratio of Specimens MS, PS2, and PS3 was less than that of
430 Specimen PS4, by approximately 35.3%, 17.6%, and 11.8% respectively, because the elastic modulus
431 of steel bolts (200 GPa) in Specimen PS4 was higher than that of CFRP bolts (100 GPa). As a result,
432 Specimen PS4 exhibited the highest stiffness among the tested specimens.

433 2.4.7 Joint openings

434 The joint opening is not expected in this precast joint type during the service condition. However,
435 when an excessive load (above the serviceability level) is applied to the joint, it may open and then
436 close after the load reduces. Joint openings of Specimens PS2, PS3, and PS4 at the top surface and
437 the bottom surface of the concrete-end-plate are shown in Fig. 18. It can be noted that the three
438 specimens using the bolts to connect beams and columns reached the maximum opening at the drift
439 ratio of 2.5%. This phenomenon may be explained that the elongation of the bolts reached the ultimate
440 values at 2.5% drift ratio and then the development of the cracks on the concrete-end-plate, the fixed
441 end, and Beam A mainly contributed to the deflection at the beam tip. Therefore, although the load-
442 carrying capacity still increased at 3% drift ratio, the joint opening slightly decreased.

443 Fig. 18 showed that the joint opening of Specimen PS4 was very small (almost zero) while those of
444 Specimens PS2 and PS3 were approximately 2.0 mm and 1.6 mm at 2.5 % drift ratio, respectively.
445 This phenomenon resulted from the effects of prestress levels in the bolts and the elastic modulus of
446 the bolts. The prestress levels in steel bolts of Specimen PS4 were approximately 51 kN while those
447 in the CFRP bolts of Specimens PS2 and PS3 were only 4.1 kN and 6.5 kN, respectively. The torsion
448 resistance of CFRP bolts was quite low so they could not be prestressed to a high level. High prestress
449 level on CFRP bolts could lead to premature damage to the bolts as shown in Fig. 19. Meanwhile, the
450 tensile forces in the top and bottom bolts at the concrete-end-plate measured by load cells during the
451 tests are shown in Fig. 20. At the drift ratio from 0.3% to 1.5%, these tensile forces in Specimens PS2
452 and PS3 were similar due to the role of the prestress forces in the initial stage. After that, the load-

carrying capacity of Specimen PS2 was higher than that of Specimen PS3. Therefore, the tensile forces in the CFRP bolts of Specimen PS2 were also higher than those of Specimen PS3. Consequently, the maximum joint opening in Specimen PS2 was higher than that of Specimen PS3 as shown in Figs. 18 and 20. It is suggested that the CFRP bolts need to be prestressed to a higher level to minimize the joint opening. Further study is deemed necessary to overcome the problem associated with the low torsion capacity of the FRP bolts.

3. Analytical calculations

In this section, the design models for beam-column joints from previous studies are adopted to examine their suitability in predicting the capacity of the precast joints using CFRP bolts and steel bolts. The examined standards include ACI 318-11 [31], NZS 3101-06 [49], BS EN 1998-1-04 [50], AIJ-2010 [51]. It is worth mentioning that all these standards and Hwang and Lee [52] model were proposed for the analysis of monolithic beam-column joints. So far, there have been no models to calculate the nominal shear capacity of the bolted precast beam-column joints. ACI 318-11 [31] recommended the following equation to calculate the nominal shear capacity of monolithic beam-column joints:

$$V_n = \gamma\sqrt{f_c'}A_j \quad (4)$$

where γ refers to a set of constants related to the confinement of the joints, γ = 1.7 for joints confined by beams on all four faces, γ = 1.2 for joints confined by beams on two or three faces, γ = 1.0 for other cases, f_c' is the compressive concrete strength, A_j is the effective joint area, and b_j and h_{col} are the effective joint width and depth, respectively, b_b *and* b_c are the width of beam and column, respectively, determination of b_b, b_c, h_{col}, and x is shown in Fig. 21,

$$A_j = b_j h_{col},\ b_j = min\{b_b + 2x,\ b_b + h_{col}\} \text{ if } b_c \geq b_b, b_j = b_c \text{ if } b_c < b_b$$

NZS 3101-06 [49] suggested the following equation to estimate the shear resistance of monolithic beam-column joints:

$$V_n = min\{0.2f_c'A_j, 10\ MPaA_j\} \quad (5)$$

where $A_j = b_j h_{col}$, b_j has the same value of b_j in the model of BS EN 1998-1-04 [50].

BS EN 1998-1-04 [50] proposed the following equation for monolithic beam-column joints:

$$V_n = \lambda\eta f_{cd}\sqrt{1 - (\frac{\upsilon_d}{\eta})}A_j \quad (6)$$

where λ depends on the joint types, λ = 1 for interior joints, λ = 0.8 for exterior joints, $\eta = 0.6\left(1 - \frac{f_c'}{250}\right)$ is the reduction factor on concrete compressive strength due to tensile strains in the transverse direction, $f_{cd} = \frac{f_c'}{1.5}$ is the design value of concrete compressive strength, υ_d is the normalized axial force in the column above the joints, $\upsilon_d = \frac{N_{Ed}}{A_c f_{cd}}$, N_{Ed} is an axial force from the analysis for the seismic design situation, A_c is the section area of the concrete column,

$A_j = b_j h_{jc}$, $b_j = min\{b_c,\ b_b + 0.5h_{col}\}$ if $b_c \geq b_b$, $b_j = min\{b_b,\ b_c + 0.5h_{col}\}$ if $b_c < b_b$, and h_{jc} is the distance between layers of column reinforcement.

AIJ-2010 [51] adopted the following equation to compute the nominal shear strength of beam-column joints:

For mean value: $$V_{n,mean} = \alpha f_c'^{\beta} A_j, \quad (7)$$

For lower value: $$V_{n,lower} = k\emptyset_j 0.8 f_c'^{0.7} A_j \quad (8)$$

where *α, β,* and *k* are based on the joint types, in which *α= 0.8, β= 0.712,* and *k= 1.0* for interior joints, *α= 0.59, β= 0.718,* and *k= 0.7* for exterior joints.

ϕ_j *= 1.0* for joints confined by beams on all four faces, ϕ_j *= 0.85* for other cases,

$A_j = b_j h_{col}$, $b_j = b_b + min\left\{\frac{b_{a1}}{2}, \frac{h_{col}}{2}\right\} + min\left\{\frac{b_{a2}}{2}, \frac{h_{col}}{2}\right\}$, values of b_b, b_{a1}, b_{a2} and h_{col} are shown in Fig. 21.

Hwang and Lee [52] suggested the following softened strut and tie model for beam-column joints:

$$V_n = K\,\zeta f_c' A_{str} cos\theta \tag{9}$$

where $K = K_h + K_v - 1$ is tie index, K_h and K_v are horizontal and vertical tie indexes for under-reinforced cases, $K_h = 1 + (\overline{K}_h - 1)F_{yh}/\overline{F}_h \le \overline{K}_h, K_v = 1 + (\overline{K}_v - 1)F_{yv}/\overline{F}_v \le \overline{K}_v$,

$\overline{K}_h = \frac{1}{[1-0.2(\gamma_h+\gamma_h^2)]}, \overline{K}_v = \frac{1}{[1-0.2(\gamma_v+\gamma_v^2)]}$, $\overline{K}_h$ and $\overline{K}_v$ are horizontal and vertical tie indexes with enough horizontal and vertical reinforcements,

$\overline{F}_h = \gamma_h \overline{K}_h \zeta f_c' A_{str} cos\theta$, $\overline{F}_v = \gamma_v \overline{K}_v \zeta f_c' A_{str} sin\theta$, $\overline{F}_h$, $\overline{F}_v$ are horizontal and vertical tie forces which horizontal and vertical ties reach yielding at failure,

$F_h = A_{th} E_s \varepsilon_h \le F_{yh}$, $F_v = A_{tv} E_s \varepsilon_v \le F_{yv}$, F_h and F_v are horizontal and vertical tie forces, F_{yh} and F_{yv} are yielding forces of horizontal and vertical ties, A_{th} and A_{tv} are the areas of horizontal and vertical ties, E_s is the elastic modulus of steel bars, ε_h and ε_v are the strains of horizontal and vertical ties, θ is the angle between the diagonal strut and the horizontal direction, γ_h, and γ_v are the force distribution coefficient, $\gamma_h = \frac{2tan\theta - 1}{3}, \gamma_v = \frac{2cot\theta - 1}{3}$, ζ is the softening coefficient, $\zeta \approx 3.35/\sqrt{f_c'} \le 0.52$, $A_{str} = a_s b_s$, a_s and b_s are the depth and width of the diagonal strut, respectively,

$$a_s = a_c = \left(0.25 + 0.85\frac{N}{A_g f_c'}\right) h_{col} \tag{10}$$

The effective area A_j, presented in ACI 318-11 [31], NZS 3101-06 [49], BS EN 1998-1-04 [50], AIJ-2010 [51], is shown in Fig. 21. In all the above standards, the column width b_c is often larger than the effective joint width b_j. b_j in NZS 3101-06 [49] and in BS EN 1998-1-04 [50] is the same and h_{jc} in BS EN 1998-1-04 [50] is lower than h_{col} in ACI 318-11 [31], NZS 3101-06 [49], AIJ-2010 [51]. These differences lead to the effective joint areas A_j in BS EN 1998-1-04 [50] the lowest.

517 Hwang and Lee [52] model proposed an assumption to determine the effective area of the diagonal
518 struts A_{str}. The depth a_b of the compression zone in the beam was neglected in calculating a_s
519 because only a small compression zone in the beam suffered from crushing. Hence, the depth of the
520 struts can be computed by $a_s = a_c$. Additionally, the width of the diagonal strut b_s is defined as the
521 effective width b_j of joints as recommended in ACI 318-11 [31]. In ACI 318-11 [31], BS EN 1998-
522 1-04 [50], and AIJ-2010 [51], the effects of the confinement from the adjacent beams were
523 investigated, whereas those effects were not mentioned in NZS 3101-06 [49]. Additionally, only BS
524 EN 1998-1-04 [50] considered the effect of the axial load on the column. When the axial load
525 decreases, there is an increase in the nominal shear capacity V_n in the joints (see Eq. 6). The concrete
526 compressive strength is a crucial parameter to estimate the nominal shear capacity of beam-column
527 joints. In addition, the tensile forces in the longitudinal reinforcements and the bolts were taken from
528 data of the strain gauges and the load cells to calculate the joint shear force V_{jmax} in Specimens PS3
529 and PS4. For Specimen PS2, the yield stress was used to calculate tensile forces in longitudinal
530 reinforcements due to unreliable data of strain gauges on this specimen. The data of the strain gauges
531 and the load cells are shown in Fig. 7 and Fig. 20.

532 Fig. 22 illustrates the equilibrium conditions to calculate the shear capacity (V_{jmax}) in the joint. This
533 value is determined as follows:

534 $$V_{jmax} = T_3 - T_1 \quad (11)$$

535 where T_1 is either the reaction force at column top of the monolithic specimen or tensile force in the
536 bolts of precast specimens, T_3 is the tensile force in the longitudinal reinforcements. T_1 depends on
537 *H* and *h* which are distance from T_1 of monolithic and precast specimens to central axis of the beam,
538 respectively. From the equilibrium condition, T_1 is inversely proportional to *H* and *h,* in which *H* is
539 significantly greater than *h*. This result indicates that the shear capacity (V_{jmax}) of Specimen MS is
540 higher than that of Specimens PS3 and PS4. The shear capacity in the experiment (V_{jmax}) and the

nominal shear capacity V_n of all the tested specimens are listed in Table 5. Considering the data in Table 5, Fig. 23 and Fig. 24, it is clear that the safety factor of Hwang and Lee [52] model was higher than those of all the standards.

As can be seen from Figs. 23 and 24, most of the standards and Hwang and Lee [52] model predicted the shear capacity of Specimen MS with significant errors because the main failure mode of Specimen MS occurred in the beam at the fixed end. For all the precast specimens, all the standards and Hwang and Lee [52] model predicted the nominal shear capacity of the joints with the errors up to 96.1%, as shown in Table 5. This result can be explained that the failure mechanism, which was used to calculate the nominal shear capacity V_n in the standards and Hwang and Lee [52] model, was different from the failure mechanism in these precast specimens. In all the standards, the nominal shear capacity was generally evaluated based on the diagonal compressive strut mechanism whereas the tensile cracks and the concrete crushing governed the main failure of these specimens, as discussed in the above sections. In addition, all the standards and Hwang and Lee [52] model do not consider the effects of prestress levels in the bolts. Further studies towards analytical models for this type of beam-column joint is deemed necessary.

For Specimen MS, the nominal shear capacity V_n calculated by ACI 318-11 [31], NZS 3101-06 [49], BS EN 1998-1-04 [50], lower-AIJ-2010 [51], mean-AIJ-2010 [51], and Hwang and Lee [52] model was higher than V_{jmax} about 30.2%, 84.4%, 15.7%, 28.5%, 70.1% and 8.1%, respectively. For precast specimens, the nominal shear capacity V_n of Specimen PS2 estimated by the ACI 318-11 [31], BS EN 1998-1-04 [50], and lower-AIJ-2010 [51] shows nearly the same value as V_{jmax}. Meanwhile, all the standards predicted the nominal shear capacity of Specimens PS3 and PS4 with considerable errors. The lowest error of 33.4% was for Specimen PS3 using lower-AIJ-2010 [51] while the highest error was 96.1% when using mean-AIJ-2010 [51] to estimate the capacity of Specimen PS4. Hwang and Lee [52] model predicts the nominal shear capacity of Specimens PS3 and PS4 with relatively smaller errors of 16.8% and 29.7%, respectively.

4. Conclusion

The proposed dry beam-column joints exhibited good performances and, therefore, can be potentially used in the prefabrication construction in both non-earthquake and earthquake-prone regions. From the experimental results and observations, the following conclusions were drawn.

1. CFRP bolts can well replace steel bolts to effectively mitigate corrosion problems.
2. The main failure occurred in the middle zone rather than at the top and bottom zones of the concrete-end-plates. This result is different from the observation reported in the previous study of Saqan [27].
3. The maximum applied load and effective stiffness in all the precast specimens were higher than those of the monolithic specimen by approximately 27-61% and 27-55%, respectively.
4. The ductility of Specimens PS3 and PS4 and MS was almost the same (2.2 vs 2.4). The ductility of Specimen PS2 was smaller than others due to a lack of confinement from steel spirals in the concrete-end-plate.
5. The overall dissipated energy of the precast specimens exceeded Specimen MS approximately by 45-75%. Drift ratio of all the precast specimens achieved 3% which satisfied the requirement of CSA A23.3-07 [40] and ASCE 41-06 [41] standards. Therefore, the proposed dry joint could be well applied in earthquake-prone regions.
6. The higher prestress level could not only improve the loading capacity but also reduce the joint openings of the precast beam-column joints.
7. The model recommended by ACI 318-11 [31], BS EN 1998-1-04 [50], lower-AIJ-2010 [51], and Hwang and Lee [52] predicted the nominal shear capacity of Specimens PS3 and PS4 with significant errors.

In conclusion, the proposed dry joint with CFRP bolts can effectively mitigate corrosion problems in the conventional dry joints but still meet the requirement for constructions in non-seismic and seismic-prone zones.

Acknowledgements

The authors would like to acknowledge the financial support from the Australian Research Council Laureate Fellowships FL180100196. The first author would like to acknowledge VIED Scholarship and Quy Nhon University, Vietnam for supporting his study.

Author contribution

Tuan T. Ngo: Data curation, Formal analysis, Investigation; Methodology; Visualization; Roles/Writing - original draft.

Thong M. Pham: Methodology, Project administration, Supervision, Writing - review & editing.

Hong Hao: Funding acquisition, Supervision, Project administration Writing - review & editing.

Declaration of Competing Interest

The authors declare that they have no known competing for financial interests or personal relationships that could have appeared to influence the work reported in this paper.

List of Figures

628 **List of Tables**

Nomenclature

Notations

μ	ductility value	l	distance from the loading point to the column face
A_h	area inside an absolute load-displacement hysteresis loop	N_{Ed}	axial force from the analysis for the seismic design situation
A_j	effective joint area	R	drift ratio value
a_s	depth of the diagonal strut	V_m	average peak load values
b_{a1}, b_{a2}	distance from margin of beam to margin column	V_n	nominal shear capacity
b_b	width of beam	α	coefficient is based on the kind joints
b_c	width of column	β	coefficient is based on the kind joints
b_j	effective joint width	γ	constants related to the confinement of the joints
b_s	width of the diagonal strut	Δ	vertical displacement of the beam tip at the position of the applying force
E_s	modulus of reinforcement and aluminium bar	Δ_m	average peak displacement values
f'_c	compressive strength of concrete	Δ_u	ultimate displacement
f_{ct}	tensile strength of concrete	Δ_y	displacement at yield
f_u	ultimate strength of reinforcement and aluminium bar	ζ	softening coefficient
f_y	yield strength of reinforcement and aluminium bar	θ	angle between diagonal strut and horizontal direction
h_{col}	effective joint depth	λ	coefficient is based on the kind joints
h_{jc}	distance between layers of column reinforcement	ξeq	equivalent viscous damping ratio
k	coefficient is based on the kind joints	υ_d	normalised axial force in the column above the joints
K	strut and tie index	ϕ_j	constants related to the confinement of the joints
K_{eff}	secant stiffness	γ_h, γ_v	force distribution coefficient

638 **Table 1**

639 Steel reinforcements and aluminium bars properties.

Bar size (mm)	Area (mm^2)	f_y (MPa)	f_u (MPa)	E_s (GPa)	Remarks
8	50	377	522	200	Spirals
10	78	560	675	200	Stirrups
16	201	597	706	200	Longitudinal reinforcements
6.3	31	110	150	69	Measuring the strain of concrete inside the concrete-end-plates

640

641

642 **Table 2**

643 Properties of CFRP bolts, nuts and plates.

Type	Dimension	Weight	Tensile strength	Shear strength	Bending strength	Compressive strength	Ultimate load	Elastic modulus	Impact strength
	mm	g	MPa	MPa	MPa	MPa	kN	GPa	kJ/M^2
Bolts	D20	376	≥ 850	≥ 160	480	760	≥ 267	100	185
Nuts	N20	44	-	-	-	-	100	100	-
Plates	150×90×20	540	-	-	-	-	≥ 100	100	-

644 Note: - = not given

645

646

647 **Table 3**

648 Load-carrying capacity and drift ratios of all the tested specimens.

Specimen	Peak load (kN)		Increase (%)		Average (kN)	Increase (%)	Drift ratio at peak load (%)	
	Push	Pull	Push	Pull			Push	Pull
MS	25.8	32.3	-	-	29.1	-	5.0	5.0
PS2	39.9	39.0	54.6	20.8	39.5	35.8	3.0	3.0
PS3	35.8	37.7	38.6	16.9	36.8	26.6	3.0	3.0
PS4	50.3	43.3	94.7	34.3	46.8	61.2	3.0	3.0

649 Note: - = not applicable

650

651 **Table 4**

652 Displacement and ductility of all the tested specimens.

Specimen	Force	H_u	$0.75H_u$	Δ_y	$0.85H_u$	Δ_u (85%)	$\mu=\Delta_u/\Delta_y$	Average (μ)	Decrease (%)
		kN	kN	mm	kN	mm			
MS	Push	25.8	19.4	15.6	22.0	35.8	2.3	2.4	-
	Pull	32.3	24.2	14.5	27.4	35.6	2.5		
PS2	Push	39.9	29.9	14.2	33.9	21.5	1.5	1.7	-29.2
	Pull	39.0	29.3	12.0	33.2	22.4	1.9		
PS3	Push	35.8	26.9	12.2	32.2*	27.5*	2.3	2.1	-12.5
	Pull	37.7	28.3	11.1	34.0*	21.5*	1.9		
PS4	Push	50.3	37.7	11.4	45.3*	26.5*	2.3	2.3	-4.2
	Pull	43.3	32.5	11.4	39.0*	26.3*	2.3		

653 ***Note**:* - = not applicable

654 * at 90% of the post-peak load

655

656

657 **Table 5**

658 The values of V_{jmax} from the experiment and V_n in the standards.

Specimens	V_{jmax} (kN)	ACI (V_n)	%	NZS (V_n)	%	EN (V_n)	%	Hwang (V_n)	%	AIJ		% Lower	% Mean
										(V_n), lower	(V_n), mean		
MS	166.6	216.9	30.2	307.2	84.4	192.7	15.7	180.1	8.1	214.1	283.4	28.5	70.1
PS2	174.5	185.9	6.5	230.4	32.0	184.5	5.7	160.7	-7.9	183.6	243.0	5.2	39.2
PS3	137.6	185.9	35.1	230.4	67.4	184.5	34.1	160.7	16.8	183.6	243.0	33.4	76.6
PS4	123.9	185.9	50.0	230.4	85.9	184.5	48.9	160.7	29.7	183.6	243.0	48.1	96.1

659

660

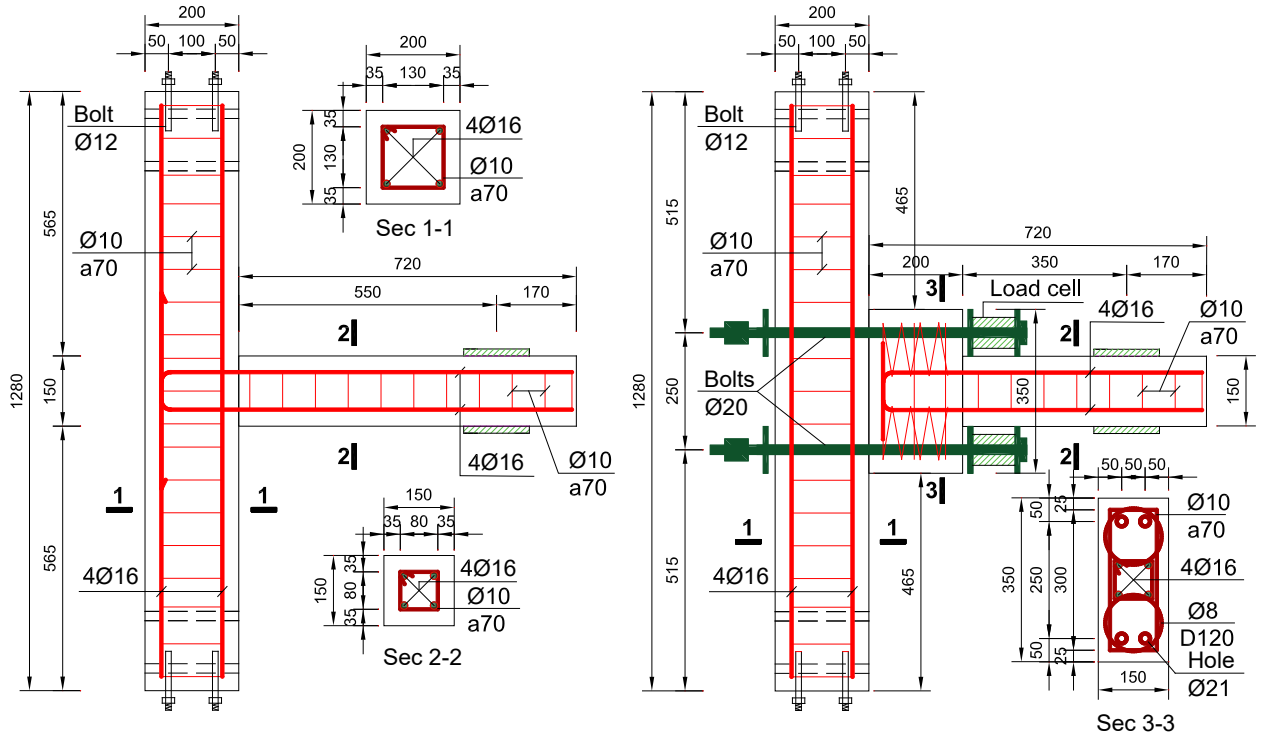

661

662 **Fig. 1.** Design of the monolithic and dry precast joints (in millimeter).

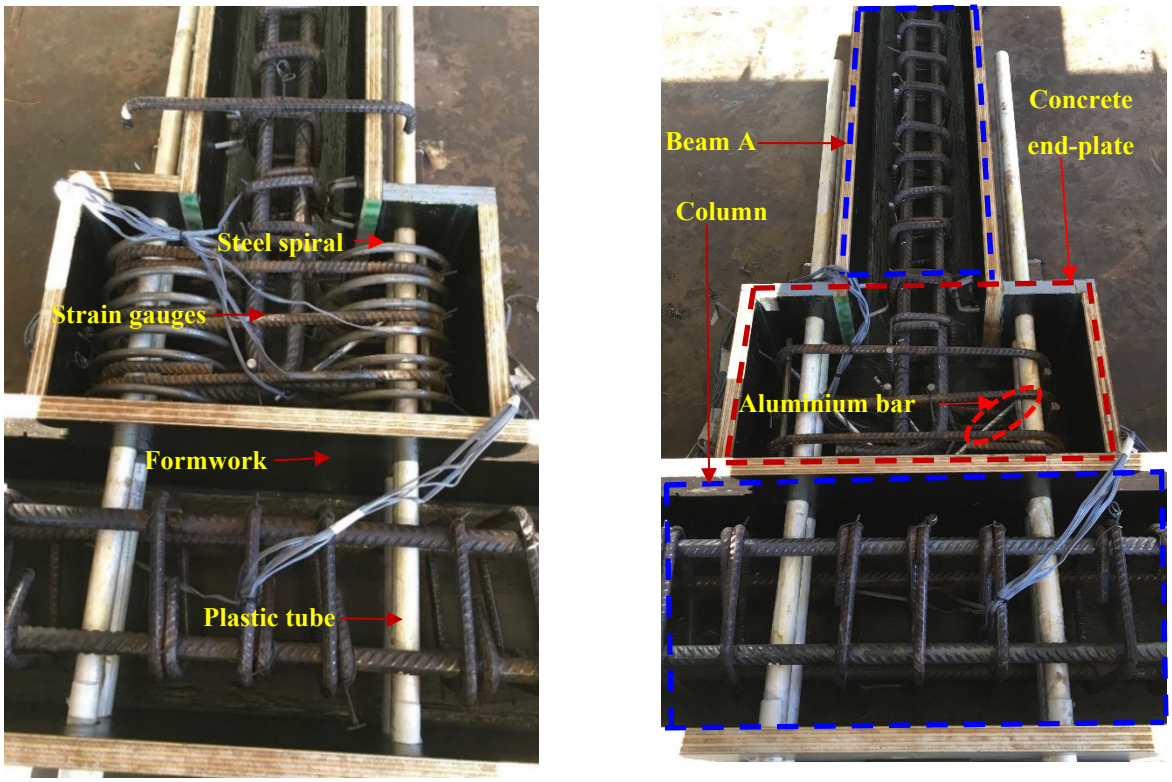

663 **Fig. 2.** Details of the reinforcements, strain gauges, aluminium bars, formworks, and plastic tubes.

664

665 **Fig. 3.** Details of strain gauges and load cells.

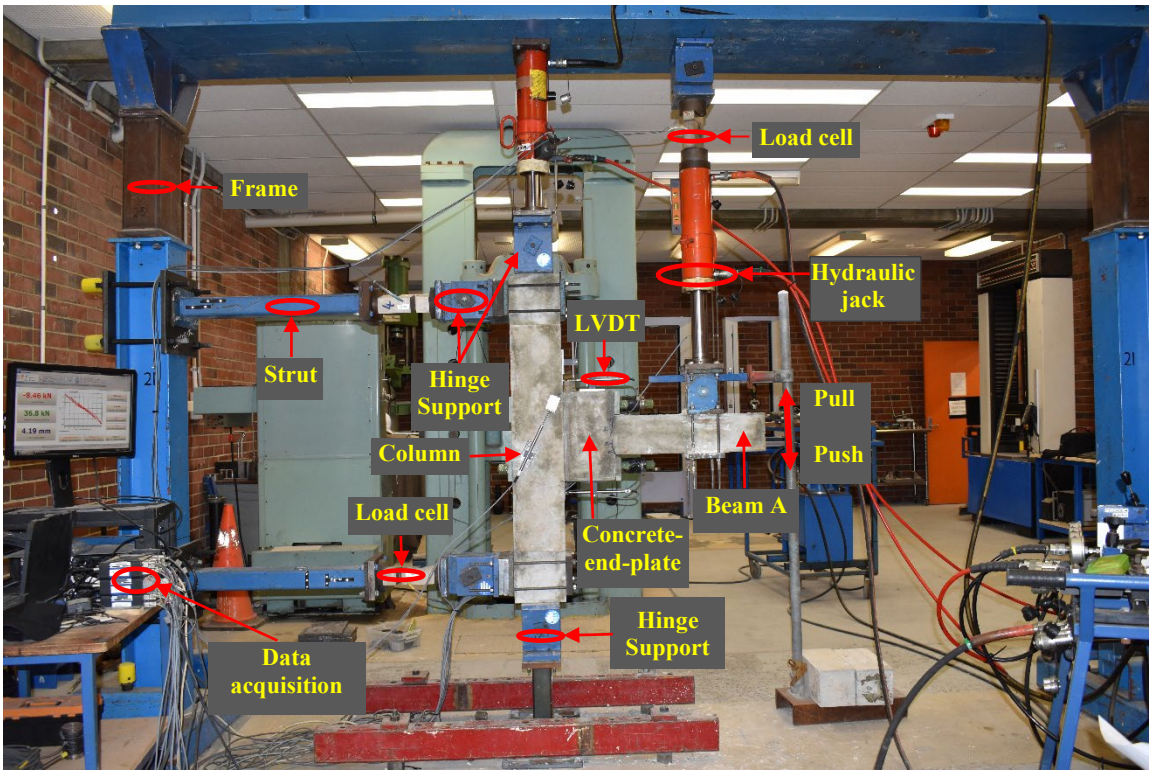

666 **Fig. 4.** A typical test setup.

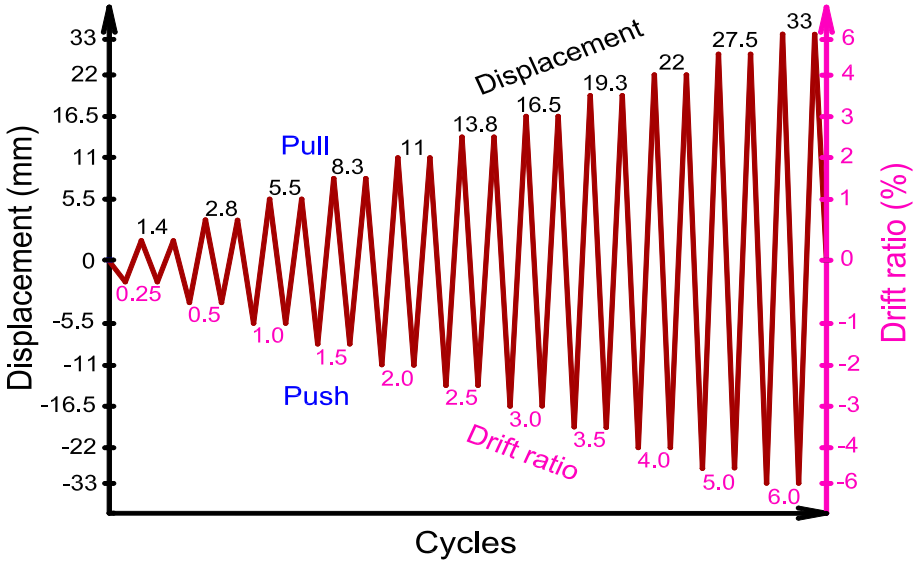

667

668 **Fig. 5.** Loading history.

669

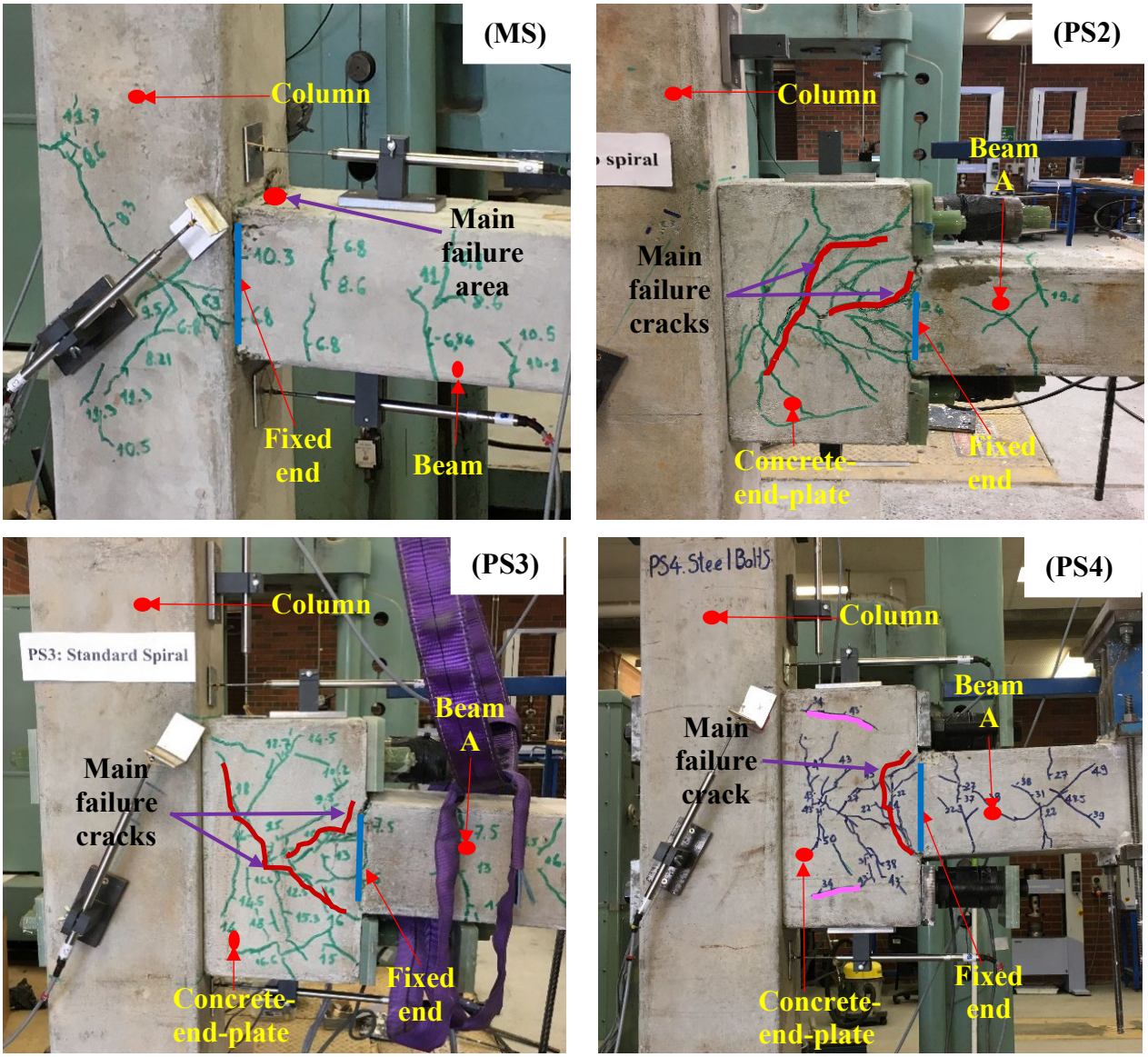

670 **Fig. 6.** Failure modes.

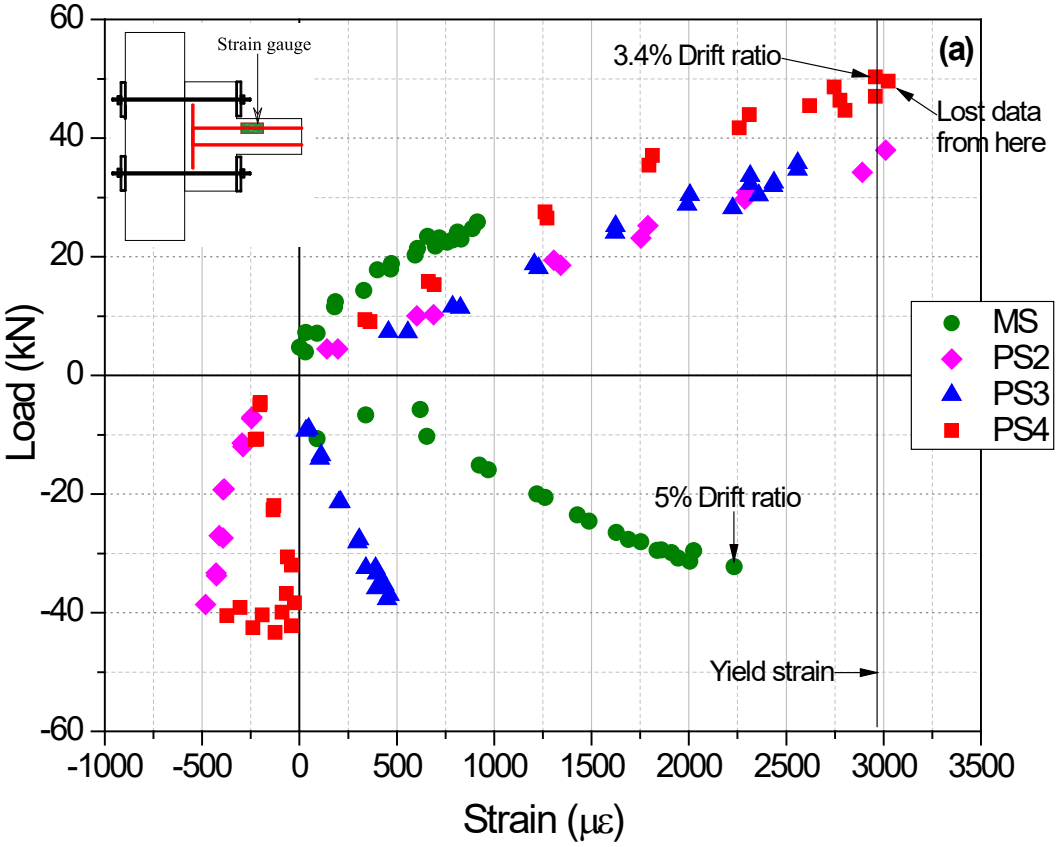
Strain gauge
3.4% Drift ratio
(a)
Lost data
from here
MS
PS2
PS3
PS4
5% Drift ratio
Yield strain
Load (kN)
Strain (με)
60
40
20
0
-20
-40
-60
-1000
-500
0
500
1000
1500
2000
2500
3000
3500

671

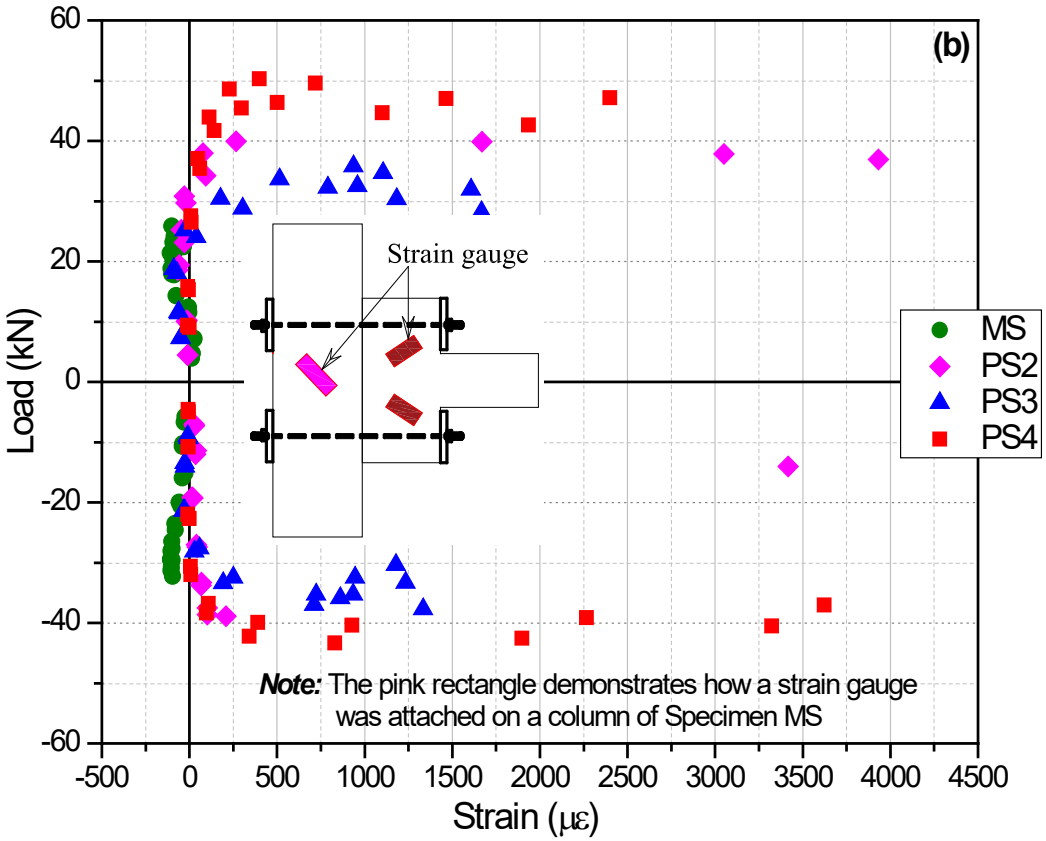

672

673 **Fig. 7.** Strain of longitudinal reinforcement (a) and on concrete (b).

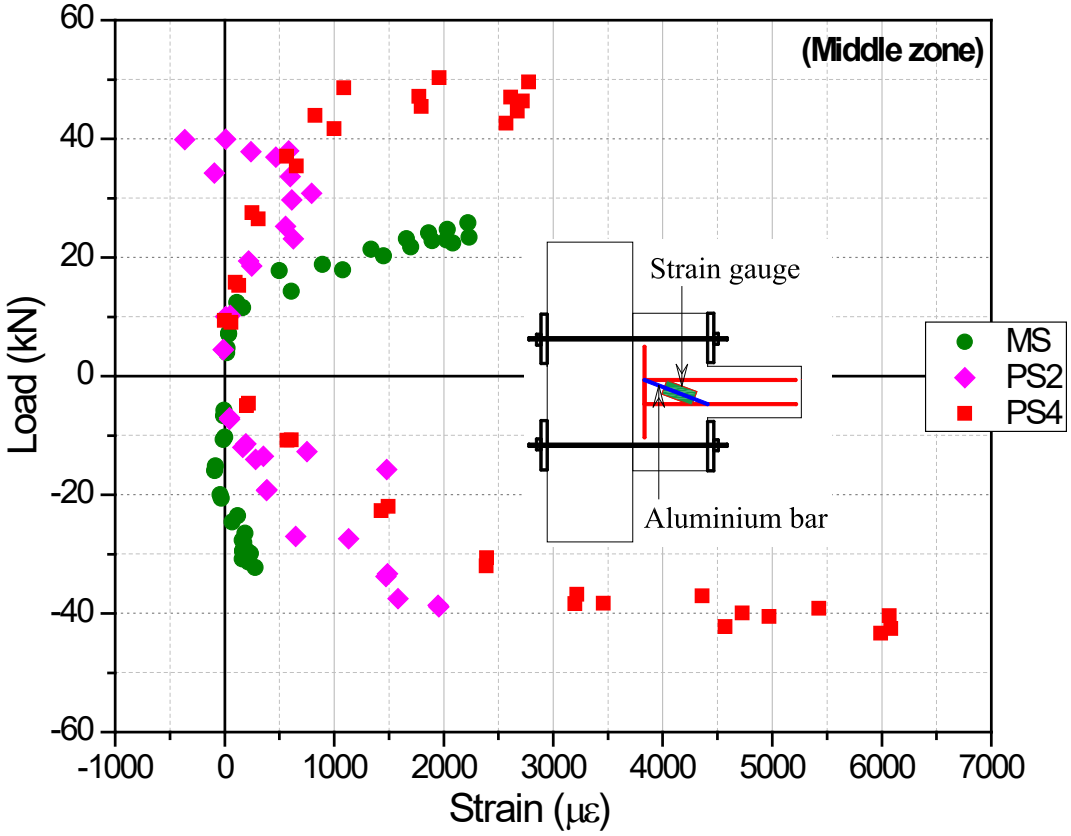
(Middle zone)
Load (kN)
Strain (με)
60
40
20
0
-20
-40
-60
-1000
0
1000
2000
3000
4000
5000
6000
7000
Strain gauge
Aluminium bar
MS
PS2
PS4

674

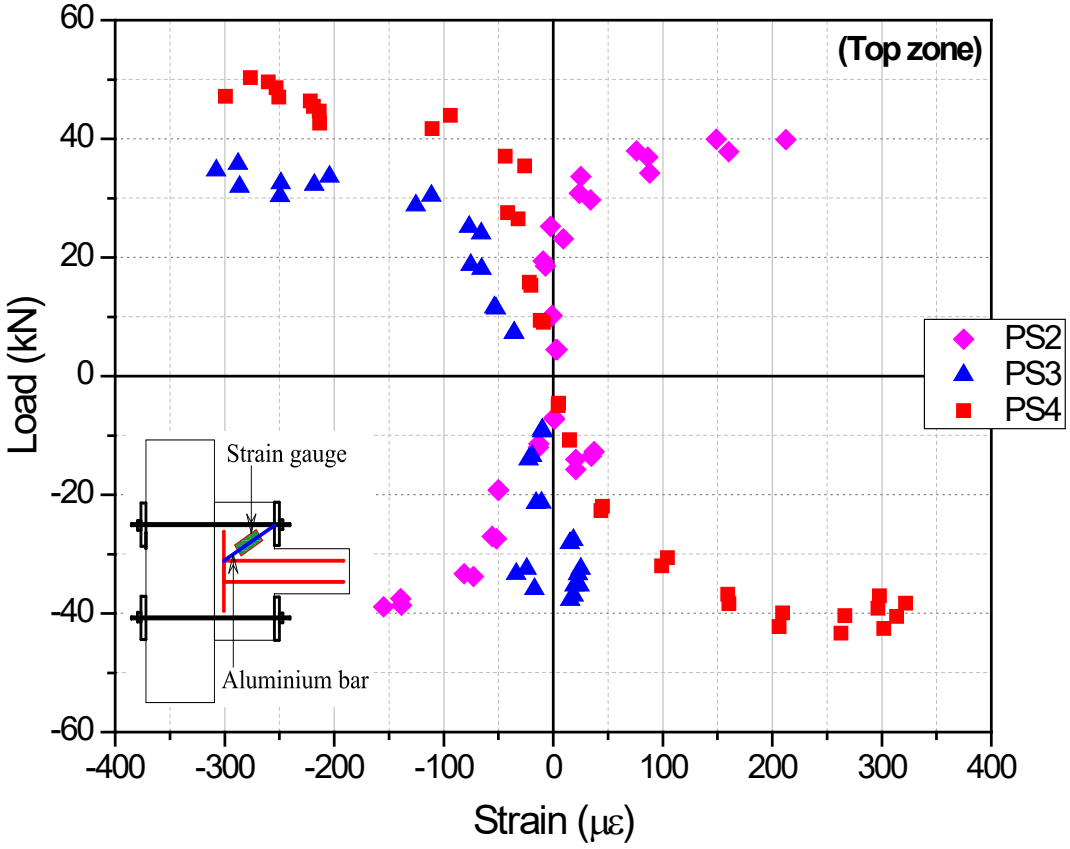

675

676 **Fig. 8.** Load versus strain of the strain gauges in the aluminium bars.

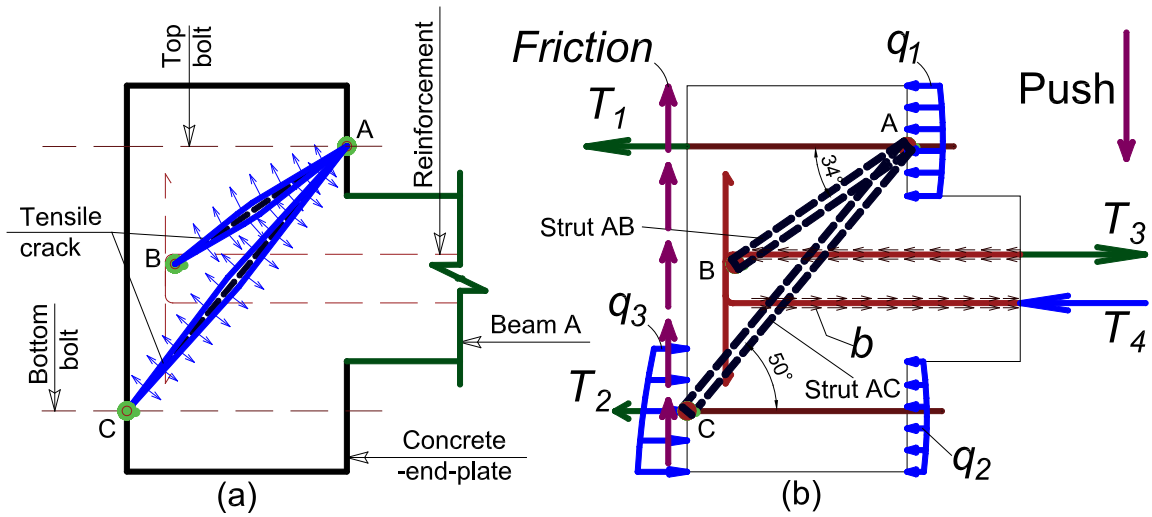

677

678 **Fig. 9.** Force path and cause of inclined cracks.

679

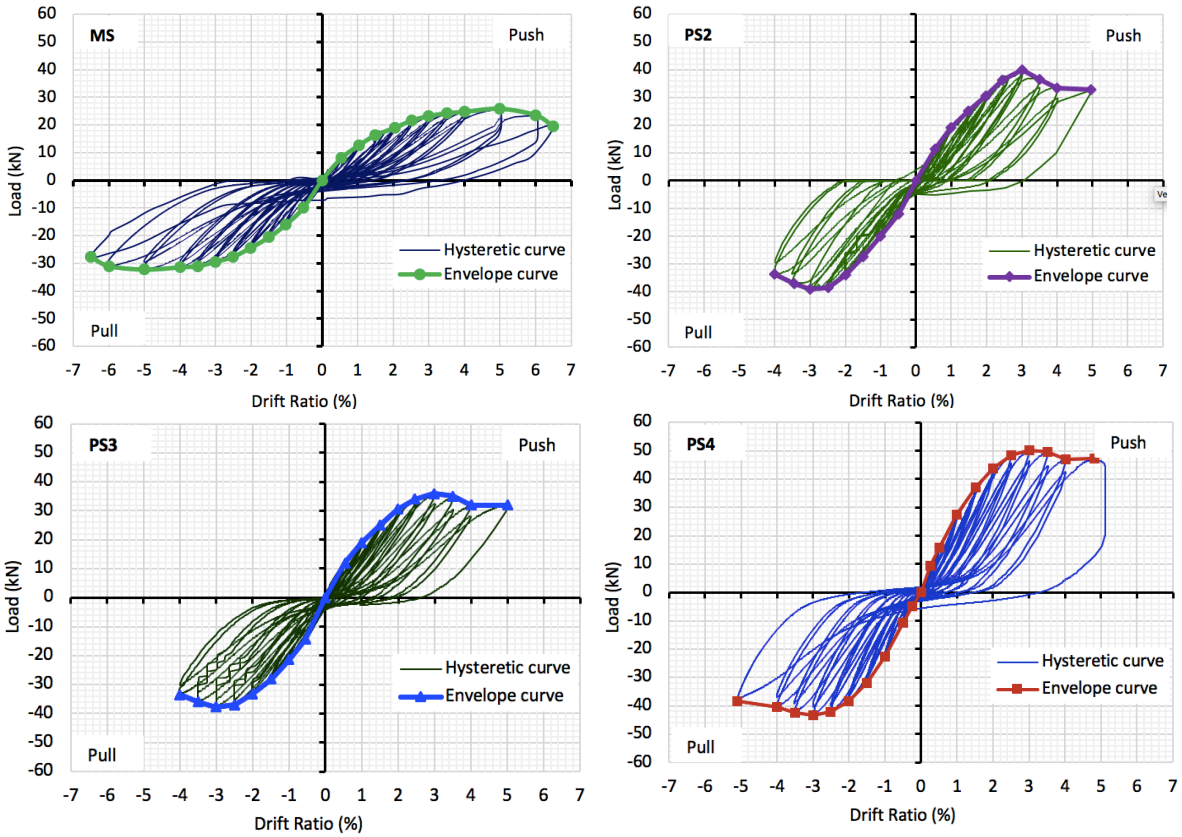

680 **Fig. 10.** Load-displacement hysteretic responses of tested specimens.

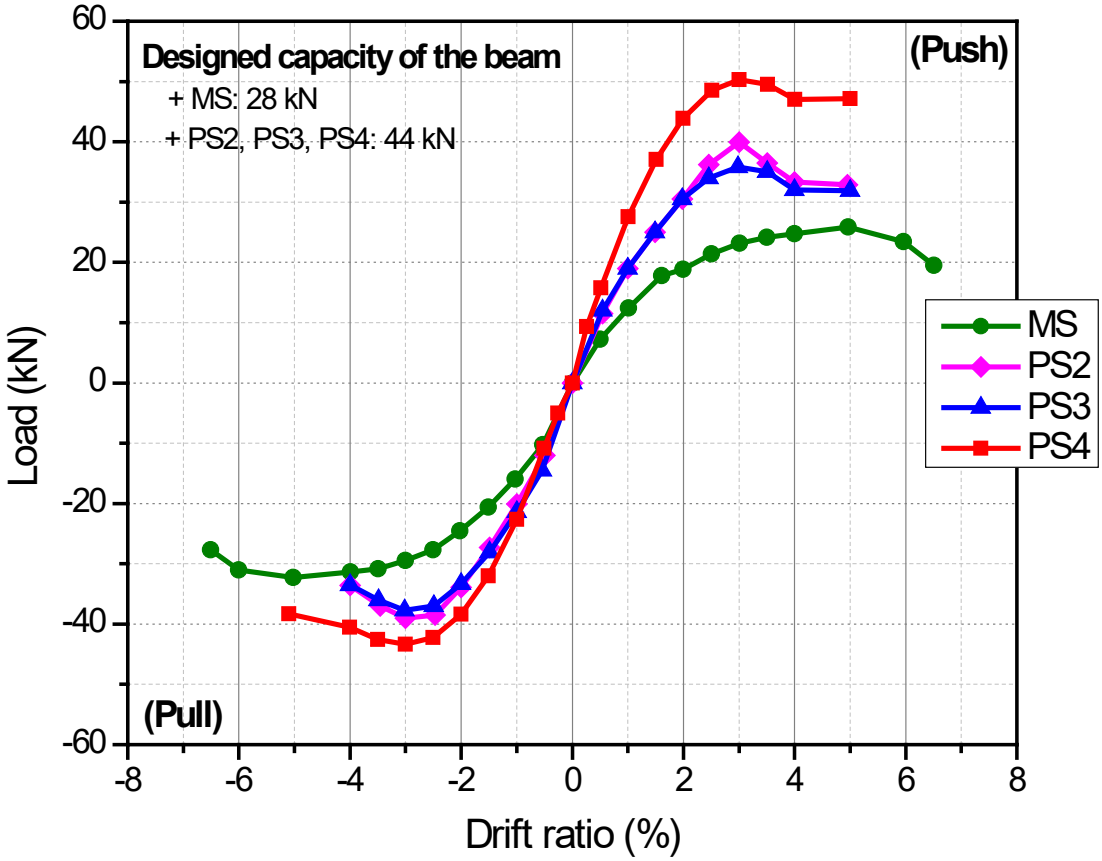

681

682 **Fig. 11.** Envelopes of hysteretic curves of all the specimens.

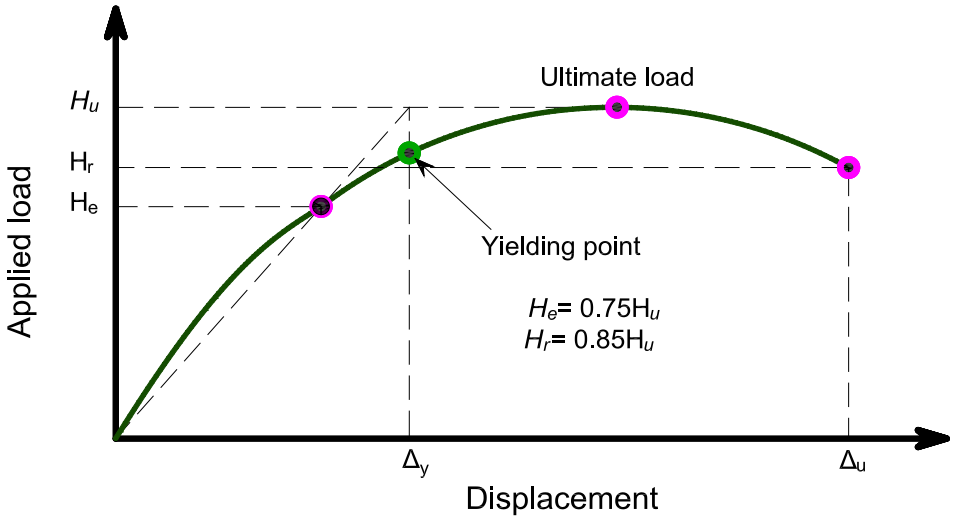

683

684 **Fig. 12.** Definitions of the yield displacement and the ultimate displacement.

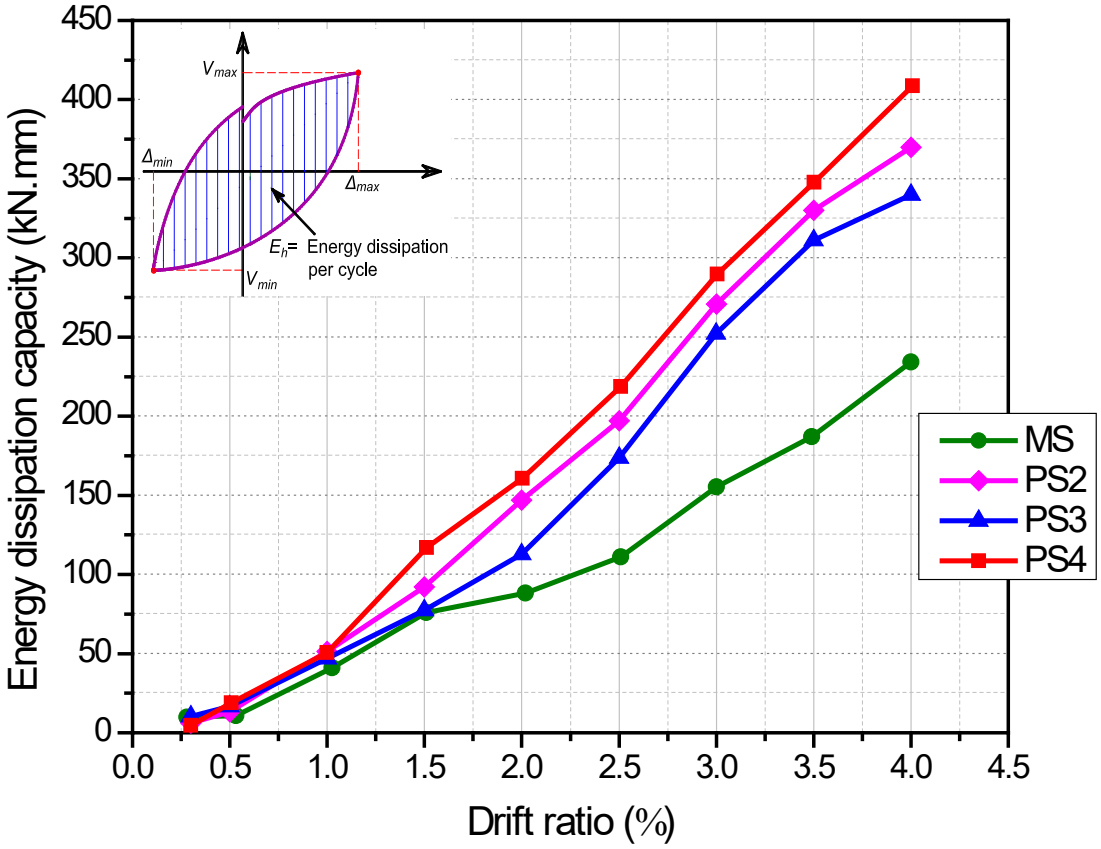

685

686 **Fig. 13.** Energy dissipation curves of the tested specimens.

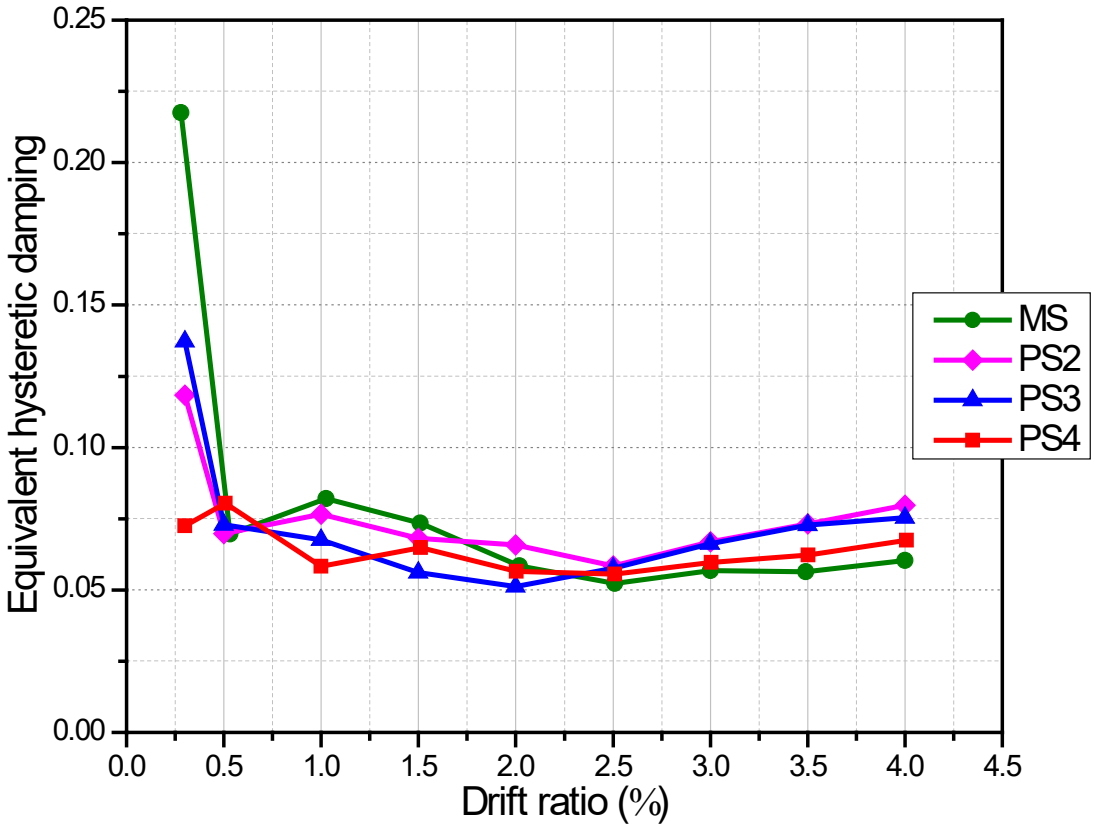

687

688 **Fig. 14.** Equivalent viscous damping ratio curves of the tested specimens.

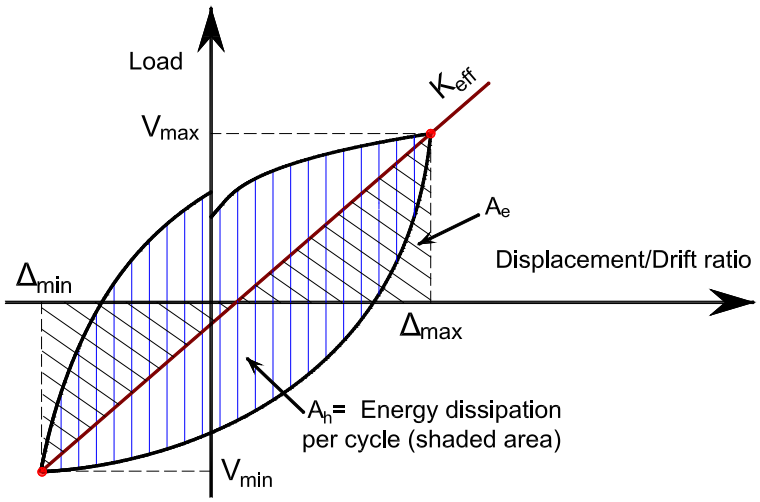

689

690 **Fig. 15.** Hysteretic energy dissipation and effective stiffness for cyclic response.

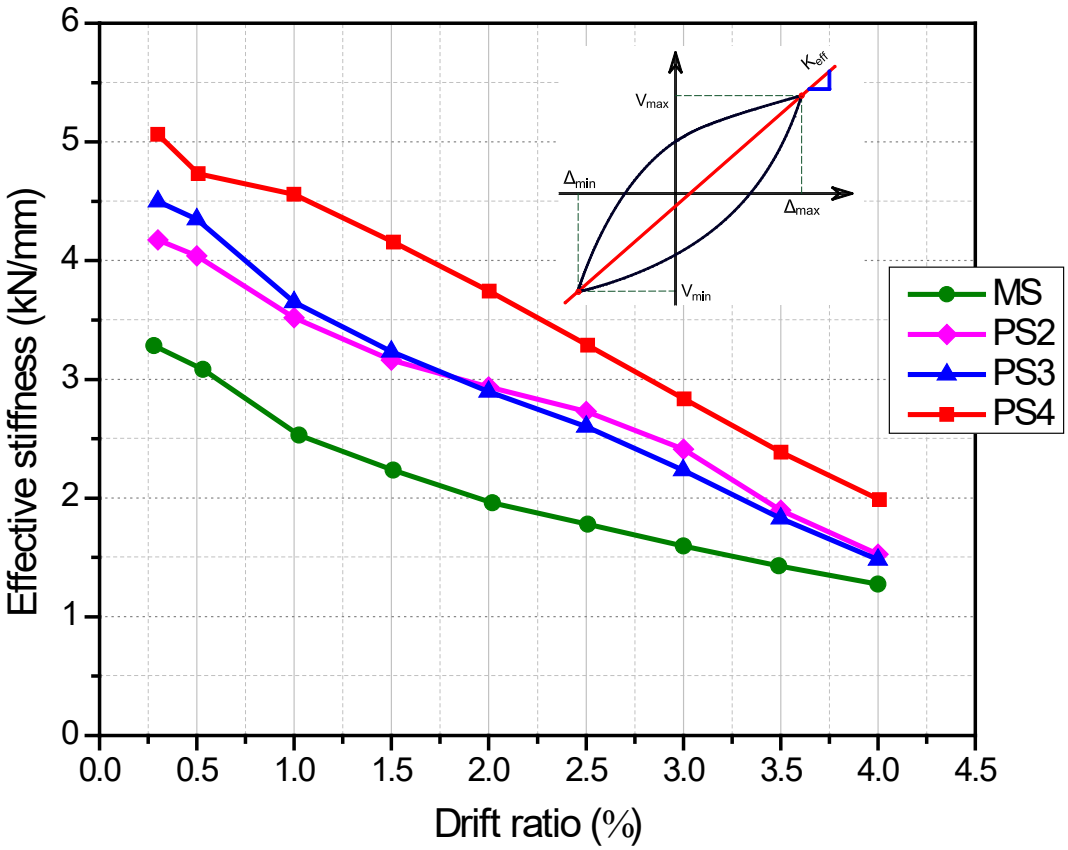

691

692 **Fig. 16.** Comparison of peak to peak stiffness.

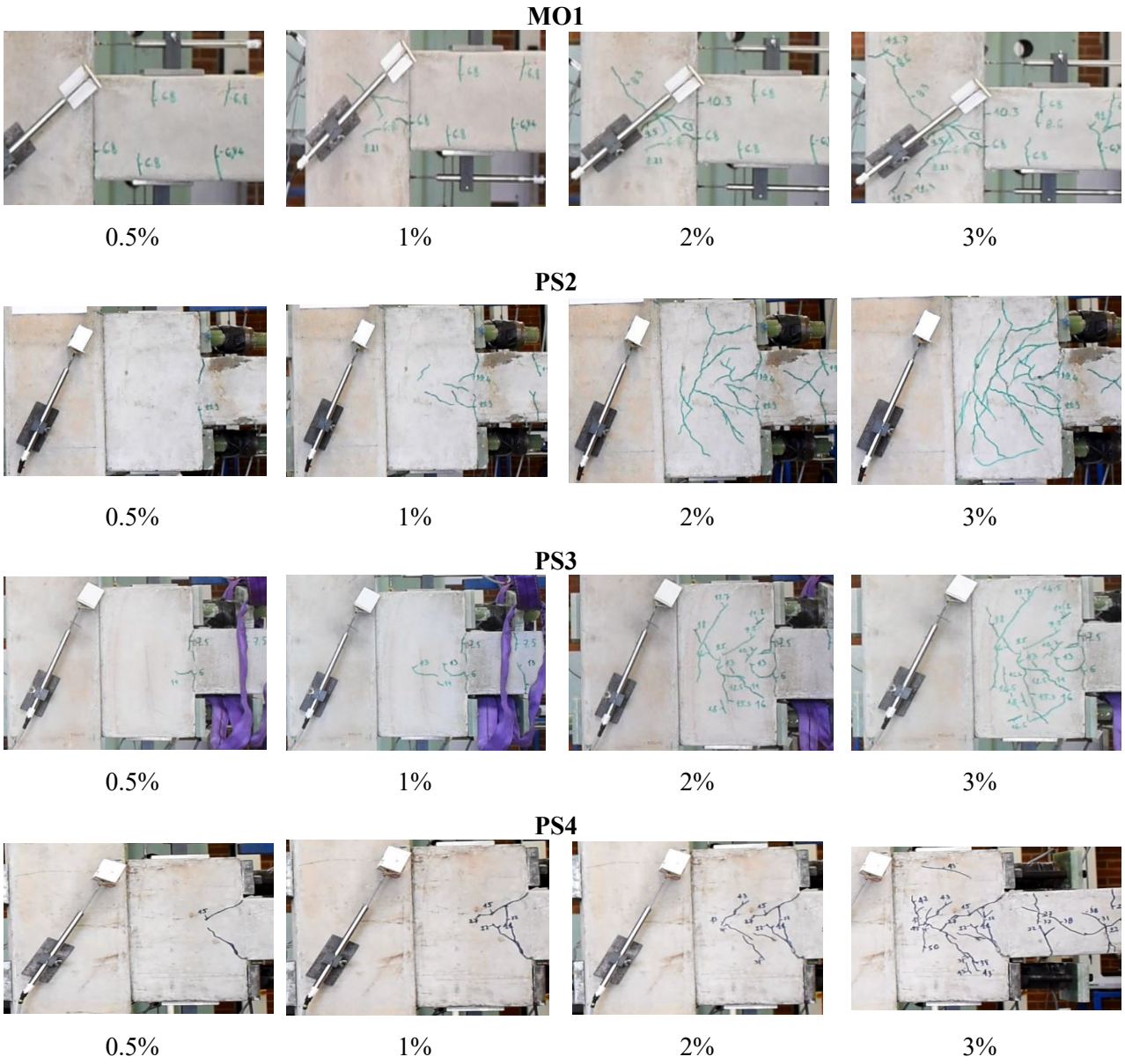

693 **Fig. 17.** The progressive failure process.

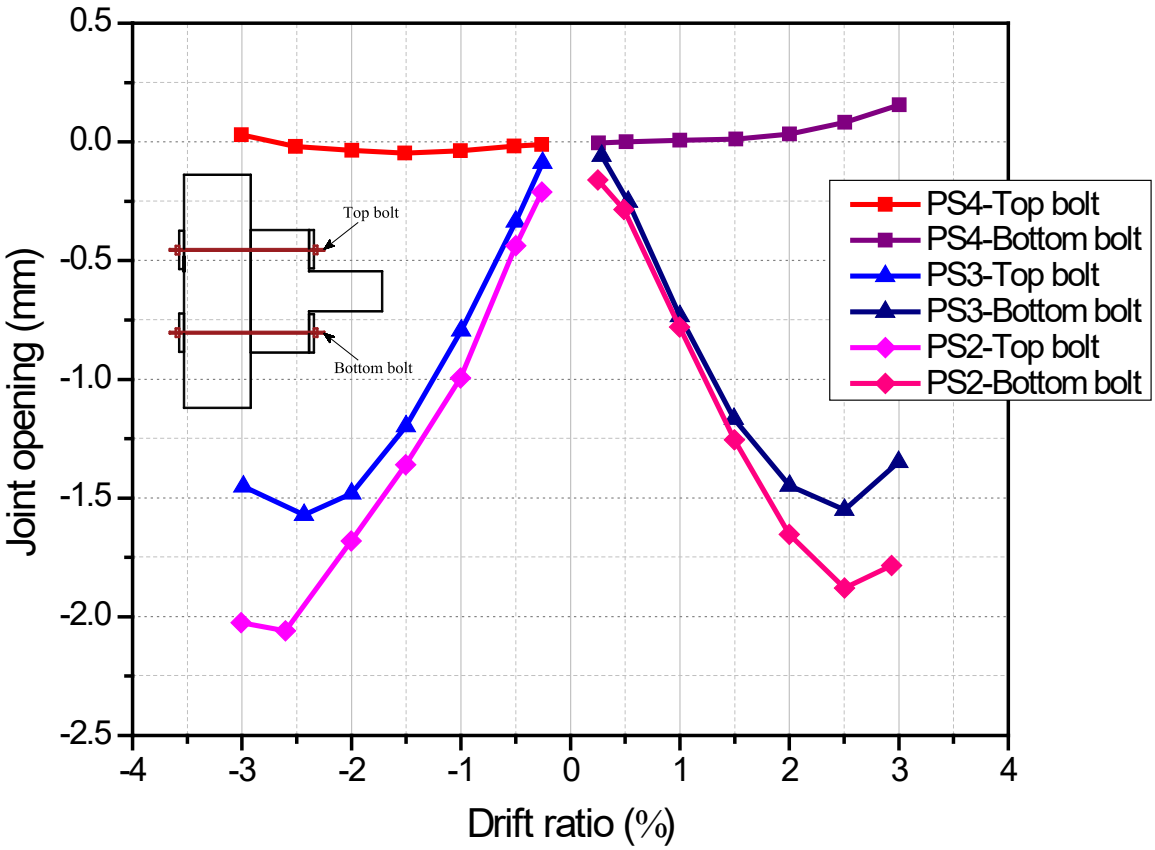

694

695 **Fig. 18.** Opening of joints at the top and bottom surface of the concrete-end-plate.

696

697 **Fig. 19.** The failure of CFRP bolts when being prestressed with a high level using a torque wrench.

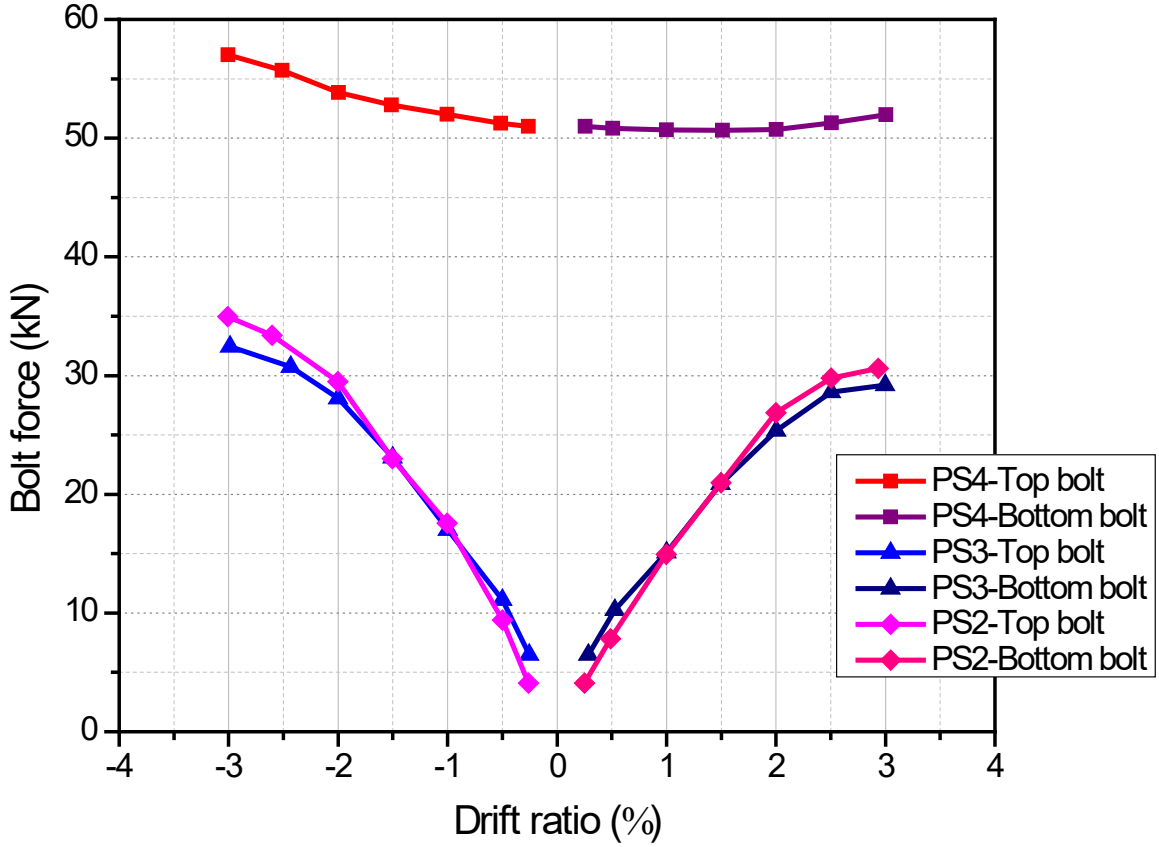

698

699 **Fig. 20.** Bolt forces at the top and bottom zone of the concrete-end-plate.

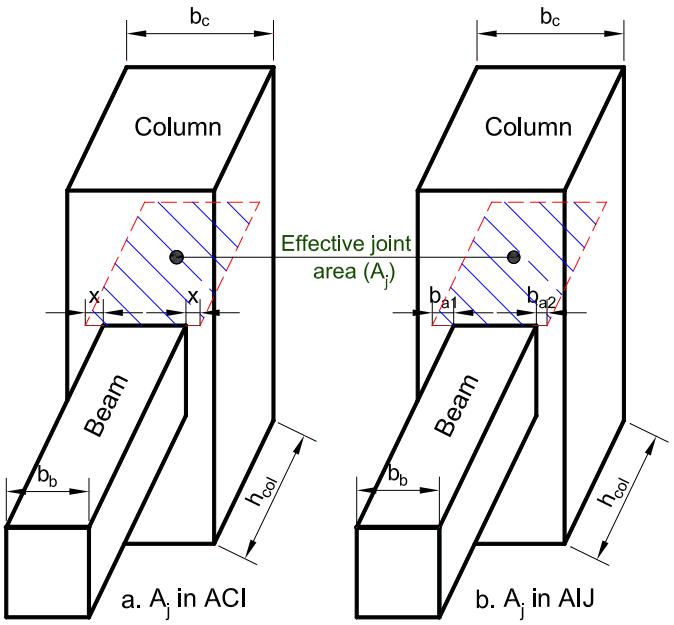

700

701 **Fig. 21.** Definition of the effective joint area.

702

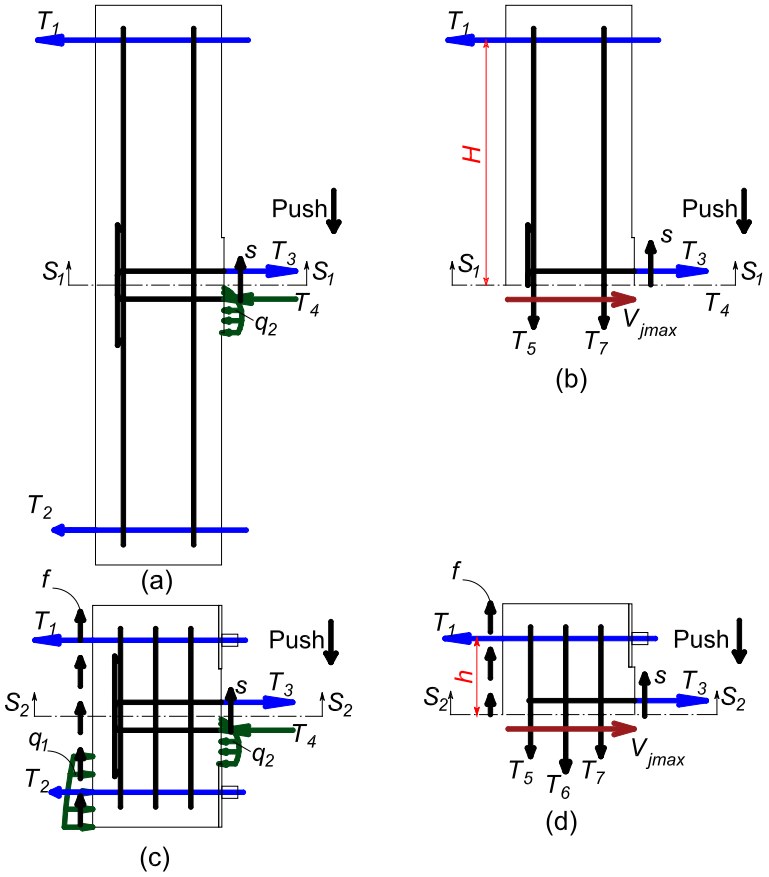

703

704 Fig. 22. Global equilibrium of exterior joints.

705

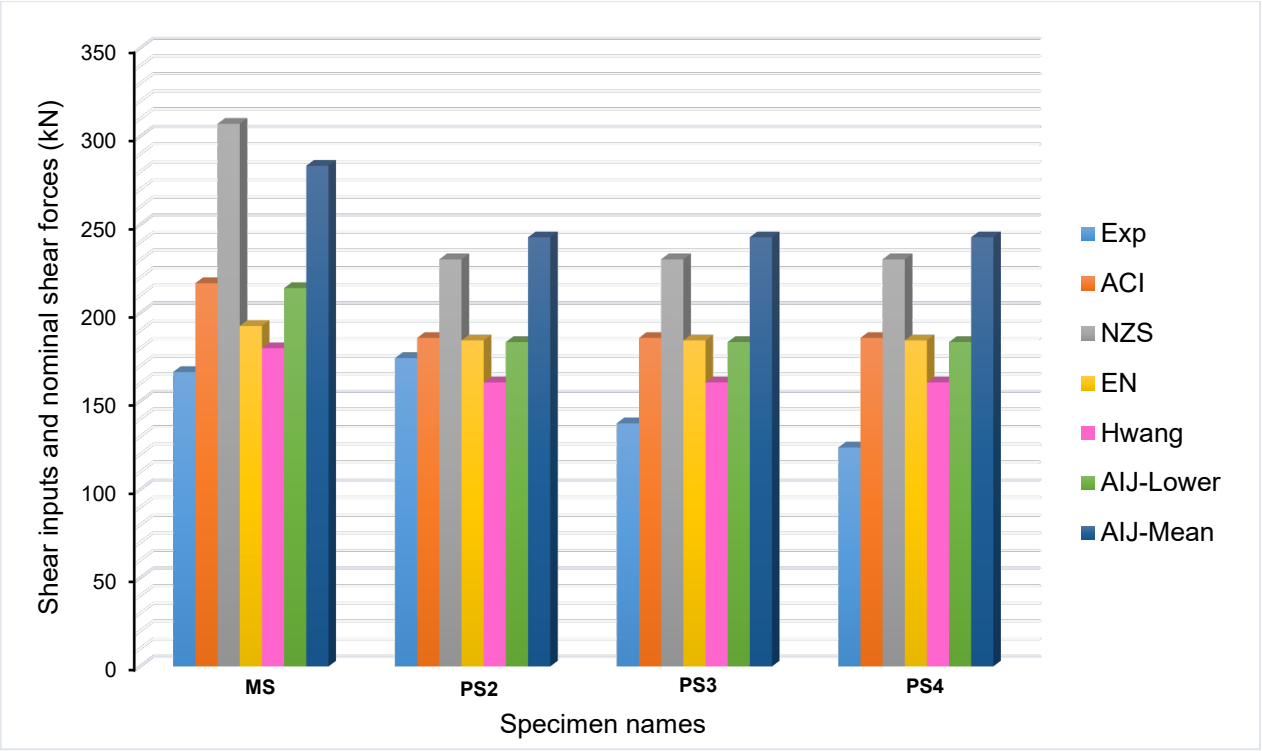

706

707 **Fig. 23.** Comparisons between the experiments and analytical results.

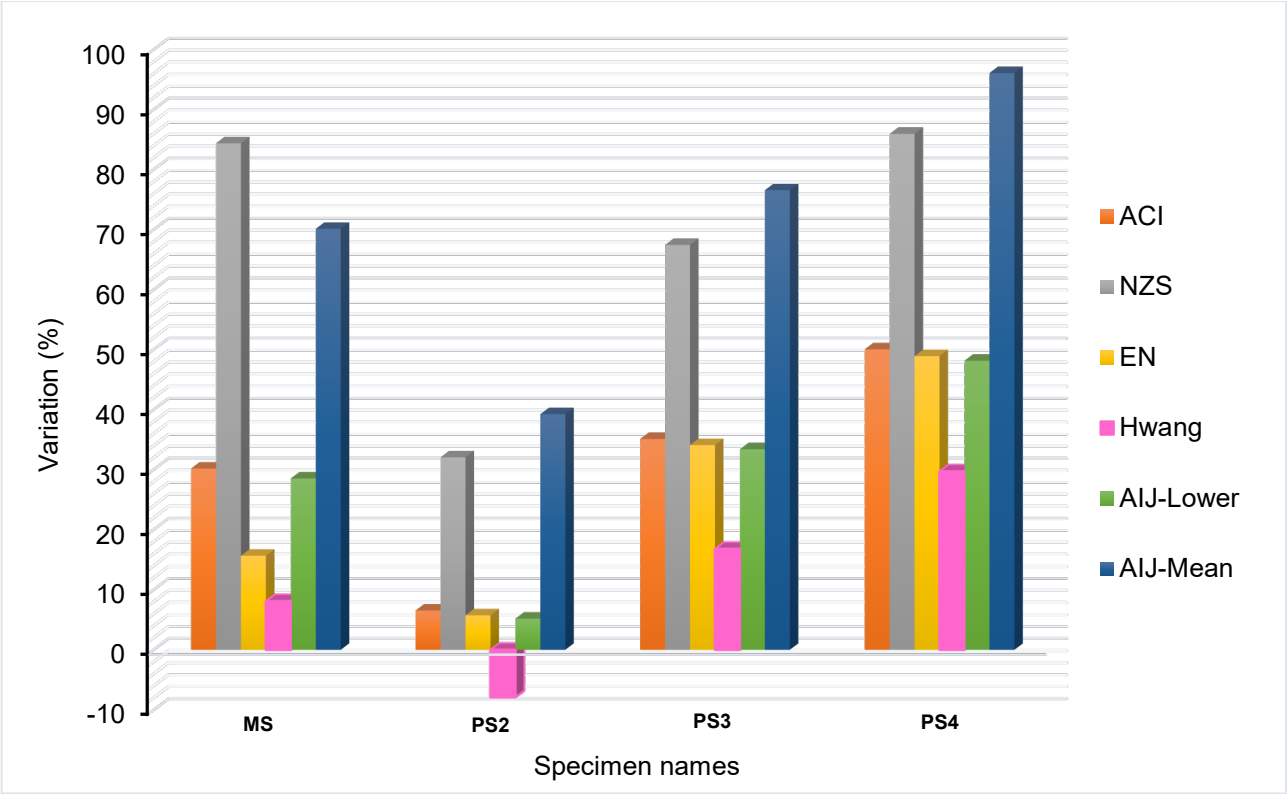

Fig. 24. Variations between the experiments and analytical results.

References

[1] Saatcioglu M. Cracking in concrete structures during the August 17, 1999 earthquake in Turkey. ACI-Special Publication 2001;204:261-76.
[2] Wang W, Li H, Wang J. Progressive collapse analysis of concrete-filled steel tubular column to steel beam connections using multi-scale model. Structures 2017;9:123-33.
[3] Bahrami S, Madhkhan M, Shirmohammadi F, Nazemi N. Behavior of two new moment resisting precast beam to column connections subjected to lateral loading. Eng Struct 2017;132:808-21.
[4] Mostofinejad D, Akhlaghi A. Flexural strengthening of reinforced concrete beam-column joints using innovative anchorage system. ACI Struct J 2017;114:1603-14.
[5] Yekrangnia M, Taheri A, Zahrai SM. Experimental and numerical evaluation of proposed precast concrete connections. Struct Concr 2016;17:959-71.
[6] Tran TM, Hadi MNS, Pham TM. A new empirical model for shear strength of reinforced concrete beam–column connections. Mag Concr Res 2014;66:514-30.
[7] Ngo TT, Pham TM, Hao H. Effects of steel fibres and prestress levels on behaviour of newly proposed exterior dry joints using SFRC and CFRP bolts. Eng Struct 2020;205:110083.
[8] Feng D-C, Wu G, Lu Y. Finite element modelling approach for precast reinforced concrete beam-to-column connections under cyclic loading. Eng Struct 2018;174:49-66.
[9] Vidjeapriya R, Jaya KP. Experimental study on two simple mechanical precast beam-column connections under reverse cyclic loading. J Perform Constr Facil 2013;27:402-14.
[10] Wouters JP, Kesner K, Poston RW. Tendon corrosion in precast segmental bridges. Transp Res Rec 1999;1654:128-32.

[11] Clifford LF. Durability of post-tensioned concrete structures. Concr Int 1991;13:58-65.
[12] Lawler N, Polak MA. Development of FRP shear bolts for punching shear retrofit of reinforced concrete slabs. J Compos Constr 2010;15:591-601.
[13] Yunovich M, Thompson NG. Corrosion of highway bridges: economic impact and control methodologies. Concr Int 2003;25:52-7.
[14] Singh V, Bansal PP, Kumar M, Kaushik SK. Experimental studies on strength and ductility of CFRP jacketed reinforced concrete beam-column joints. Constr Build Mater 2014;55:194-201.
[15] Dalalbashi A, Eslami A, Ronagh HR. Plastic hinge relocation in RC joints as an alternative method of retrofitting using FRP. Compos Struct 2012;94:2433-9.
[16] Benmokrane B, Robert M, Mohamed HM, Ali AH, Cousin P. Durability assessment of glass FRP solid and hollow bars (rock bolts) for application in ground control of jurong rock caverns in Singapore. J Compos Constr 2017;21:06016002.
[17] Li Y-m, Ma N-j, Yang K, Shi J-j. Research on FRP bolt-end failure mechanism. Mining Science and Technology (China) 2009;19:0522-5.
[18] Mady M, El-Ragaby A, El-Salakawy EF. Experimental investigation on the seismic performance of beam-column joints reinforced with GFRP bars. J Earthquake Eng 2011;15:77-98.
[19] Mady MHA. Seismic behaviour of exterior beam-column joints reinforced with FRP bars and stirrups. 395 Wellington Street, Ottawa ON K1A 0N4, Canada: University of Manitoba (Canada); 2011.
[20] Le TD, Pham TM, Hao H, Yuan C. Performance of precast segmental concrete beams posttensioned with carbon fiber-reinforced polymer (CFRP) tendons. Compos Struct 2019;208:56-69.
[21] Wang X, Shi J, Wu G, Yang L, Wu Z. Effectiveness of basalt FRP tendons for strengthening of RC beams through the external prestressing technique. Eng Struct 2015;101:34-44.
[22] Schmidt JW, Bennitz A, Täljsten B, Goltermann P, Pedersen H. Mechanical anchorage of FRP tendons – A literature review. Constr Build Mater 2012;32:110-21.
[23] Li J, Samali B, Ye L, Bakoss S. Behaviour of concrete beam–column connections reinforced with hybrid FRP sheet. Compos Struct 2002;57:357-65.
[24] Ghomi SK, El-Salakawy E. Seismic performance of GFRP-RC exterior beam–column joints with lateral beams. J Compos Constr 2016;20:04015019.
[25] Feroldi F, Russo S. Structural behavior of all-FRP beam-column plate-bolted joints. J Compos Constr 2016;20:04016004.
[26] Hanaor A, Ben-Arroyo A. Prestressed bolting in precast concrete beam-column connection. Proceedings of the institution of civil engineers: Structures and buildings: Thomas Telford Services Ltd; 1998. p. 144-53.
[27] Saqan EI. Evaluation of ductile beam-column connections for use in seismic- resistant precast frames. USA: University of Texas at Austin; 1995.
[28] Palmieri L, Saqan E, French C, Kreger M. Ductile connections for precast concrete frame systems. ACI-Special Publication 1996;162-13:313-56.
[29] ACI 550R-96. Design recommendation for precast concrete structures. ACI 550R-96. Farmington Hills, MI: ACI (American Concrete Institute); 1996. p. 115-21.
[30] ACI 352R-02. Recommendations for design of beam-column connections in monolithic reinforced concrete structures. ACI 352R-02. Farmington Hills, MI: ACI (American Concrete Institute); 2002. p. 38.00.
[31] ACI 318-11. Building Code Requirements for Structural Concrete (ACI 318-11) and Commentary. ACI 318-11,. Farmington Hills, MI 48331: American Concrete Institute; 2011. p. 503.
[32] Wight JK, MacGregor JG. Reinforced concrete: Mechanics and design. 6th ed. Boston: Boston : Pearson; 2012.
[33] AS 1012.8.1-14. Method for Making and Curing Concrete-Compression and Indirect Tensile Test Specimens. AS 10128 1-14,: Australian Standard; 2014.

[34] AS 1012.9.1-14. Methods of testing concrete-Compressive strength tests-Concrete, mortar and grout specimens. AS 101291-14,. Standards Australia. Strathfield, Australia: Australian Standard; 2014.
[35] J and R Metalwork Industry CO. L. Quotation and Properties of CFRP bolts. China2018.
[36] GB/T 1447-05. Fiber-reinforced plastics composites-Determination of tensile properties. GB/T 1447-05. China: GB (Chinese Standard); 2005.
[37] Ltd HECP. High tensile: Metric vs Imperial (bolts). Australia2018. p. 2.
[38] Antonopoulos CP, Triantafillou TC. Experimental investigation of FRP-strengthened RC beam-column joints. J Compos Constr 2003;7:39-49.
[39] ACI T1.1-01. Acceptance criteria for moment frames based on structural testing and commentary. ACI T11-01,. American Concrete Institute: ACI Committee; 2001. p. 1-7.
[40] CSA A23.3-07. Design of concrete structures. CSA A233-07,. Mississauga, Ontario, Canada: Canadian Standards Association; 2007.
[41] ASCE 41-06. Seismic rehabilitation of existing buildings. ASCE 41-06,. ASCE Reston, VA: ASCE Reston, VA; 2006.
[42] Turmo J, Ramos G, Aparicio AC. FEM modelling of unbonded post-tensioned segmental beams with dry joints. Eng Struct 2006;28:1852-63.
[43] Le TD, Pham TM, Hao H. Analytical investigation of the performance of precast segmental concrete beams internally prestressed with unbonded steel tendons. 2019:(Under review).
[44] Park R. Evaluation of ductility of structures and structural assemblages from laboratory testing. Bulletin of the New Zealand national society for earthquake engineering 1989;22:155-66.
[45] Park RL, Park R, Paulay T. Reinforced concrete structures: John Wiley & Sons; 1975.
[46] Hadi MN, Schmidt LC. Use of helixes in reinforced concrete beams. ACI Struct J 2002;99:191-8.
[47] Xue W, Zhang B. Seismic behavior of hybrid concrete beam-column connections with composite beams and cast-in-place columns. ACI Struct J 2014;111:617-27.
[48] Priestley MN, Seible F, Calvi GM. Seismic design and retrofit of bridges. 605 Third avenue, New York: John Wiley & Sons; 1996.
[49] NZS 3101-06. Concrete Structures Standard - Part 1: The design of concrete structures. NZS 3101-06,. New Zealand, Wellington: Standards New Zealand; 2006. p. 137.
[50] BS EN 1998-1-04. Eurocode 8: Design of structures for earthquake resistance - Part 1: General rules, seismic actions and rules for buildings. BS EN 1998-1-04,: European Committee for Standardization; 2004. p. 112-3.
[51] AIJ-2010. Standard for structural calculation of reinforced concrete structures. Tokyo, Japan: Architectural Institute of Japan; 2010. p. 179-82.
[52] Hwang S-J, Lee H-J. Strength prediction for discontinuity regions by softened strut-and-tie model. J Struct Eng 2002;128:1519-26.